Influence of cell mechanics in embryonic bile duct lumen formation: insight from quantitative modeling

Paul van Liedekerke, Lila Gannoun, Axelle Loriot, Frédéric P Lemaigre, Dirk Drasdo

To cite this version:

Paul van Liedekerke, Lila Gannoun, Axelle Loriot, Frédéric P Lemaigre, Dirk Drasdo. Influence of cell mechanics in embryonic bile duct lumen formation: insight from quantitative modeling. 2021. hal-03135722

HAL Id: hal-03135722
https://inria.hal.science/hal-03135722v1

Preprint submitted on 9 Feb 2021

Influence of cell mechanics in embryonic bile duct lumen formation: insight from quantitative modeling

Paul Van Liedekerke[1,2☯], Lila Gannoun[2☯], Axelle Loriot[2], Frédéric P. Lemaigre[2‡], Dirk Drasdo[3‡]

1 Modelling and Analysis for Medical and Biological Applications (MAMBA), Inria Paris Sorbonne Université LJLL, 2 Rue Simone IFF, 75012 Paris, France.
2 de Duve Institute, Université Catholique de Louvain, Avenue Hippocrate 75/B1-7503, 1200 Brussels, Belgium
3 Leibniz Research Centre for Working Environment and Human Factors at the Technical University Dortmund, 44139 Dortmund, Germany.

☯These authors contributed equally to this work.
‡Co-senior authorship.
Corresponding authors: Paul.Van_Liedekerke@inria.fr, Dirk.Drasdo@inria.fr

Abstract

In biological and medical literature, alternative hypotheses for initial bile duct lumen formation during embryogenesis exist, which so far remained largely untested. Guided by the quantification of morphological features and expression of genes in developing bile ducts from embryonic mouse liver, these hypotheses were sharpened and data collected that permitted to develop a high resolution individual-based computational model to test the alternative hypotheses in silico. Simulations with this model suggest that successful bile duct lumen formation primarily requires the simultaneous contribution of directed cell division of cholangiocytes, local osmotic effects generated by salt excretion in the lumen, and temporally-controlled differentiation of hepatoblasts to cholangiocytes, with apical constriction of cholangiocytes only moderately affecting luminal size.

Author summary

The initial step in bile duct development is the formation of a biliary lumen, a process which involves several cellular mechanisms, such as cell division, secretion of fluid, and polarization. However, orchestrating these mechanisms in time and space is complex and difficult to validate. Therefore, we built a computational model of biliary lumen formation. The model represents every cell and function at high detail. With the model we can simulate the effect of physical aspects that affect the duct formation processes. Here, we have tested the individual and combined effects of directed cell division, apical constriction, and osmotic effects on lumen growth by varying the parameters that control their relative strength. Simulations with our model suggest that successful bile duct lumen formation primarily requires the simultaneous contribution of directed cell division of cholangiocytes, local osmotic effects generated by salt excretion in the lumen, and temporally-controlled differentiation of hepatoblasts to cholangiocytes, with apical constriction of cholangiocytes only moderately affecting luminal size.

Introduction

In embryonic liver, cholangiocytes and hepatocytes differentiate from bipotent hepatoblasts. Differentiation of cholangiocytes is spatially restricted around the mesenchyme associated with the branches of the portal vein [1, 2]. The conversion of hepatoblasts to cholangiocytes is induced by cell-cell contacts between the mesenchymal cells and adjacent hepatoblasts, as well as by factors secreted by the mesenchyme which target receptors at the membrane of the hepatoblasts [3].

Hepatoblasts that have differentiated to cholangiocytes initially constitute a "ductal plate", which is a discontinuous and single-layered sheet of cholangiocytes located near the portal mesenchyme (Fig 1A,C). Duct morphogenesis is then initiated by the appearance of several lumina delineated on the portal side by ductal plate cholangiocytes, and on the parenchymal side by hepatoblasts. Therefore, the initial ductal structures are lined by two distinct cell types. When duct formation proceeds, the hepatoblasts which delineate the parenchymal side of the lumina progressively differentiate to cholangiocytes [2–7].

Bile duct lumen formation proceeds according to a cord hollowing process which consists in the appearance of a lumen between adhering cells [4, 7, 8]. Lumenogenesis implies that the cells, which delineate an apical lumen coordinately undergo apico-basal polarization and develop adhesive junctions [9, 10]. A space can form between the apical surfaces of cells that face each other, as a result of repulsive forces, exocytosis of vesicles containing luminal components, or accumulation of fluid. Fluid leakage should then be prevented by junctional complexes between the cells that delineate the apical luminal space. Putting these notions in the context of biliary lumen formation, earlier work has shown that cholangiocytes develop apical poles when they start forming the ductal plate (Fig 1C). Polarization is initiated in single cholangiocytes and extends to adjacent cholangiocytes, likely via Notch and Neurofibromin 2 signaling. The cholangiocytes then coordinately and collectively contribute to delineate a lumen together with hepatoblasts [4, 7, 11]. Still, the driving forces allowing lumen formation remain unclear.

Computational models offer means to simulate a set of hypothesized mechanisms free from unknown influences and identify whether this set is either able or fails to explain experimental observations, which in the latter case indicates missing or false hypotheses. Over the past years, a class of computational models, called agent-based models (ABM), have been increasingly deployed to better understand the role of mechanics in tissue growth, regeneration and development. In ABMs of tissues, each cell is represented individually and is characterized by its behavior as well as by state changes. For example, a cell may be able to grow, divide, migrate, and undergo state changes, whereby the state might represent a cell type, activation state, etc. Cell dynamics and state are formalized by mathematical rules or equations. Parameters at the cell-level may be functions of intracellular molecular processes such as e.g. signaling events. ABMs have been explored in discrete and continuum space. In continuum space, a first large class of ABM are called center-based models (CBM), in which a cell shape is rigid and geometrically approximated by an object that represents a coarse-grained description of cell shape only in a statistical sense by occupying a region in space where most of the cell volume is located [12–21]. A second class can be largely categorized as "deformable" models, e.g [22–34], in which cell shape is resolved explicitly, hence permitting a much more accurate representation of the interplay of cell shape and forces on the cell. The use of deformable models may be considered as mandatory in cases where cell shape is assumed to be a critical determinant, for example, driving or controlling local cell arrangements.

At the onset of biliary morphogenesis, very small lumina and a high variability in cell shapes are observed close to the formed lumina, meeting precisely the aforementioned conditions. For these reasons, we employ a high resolution model for the

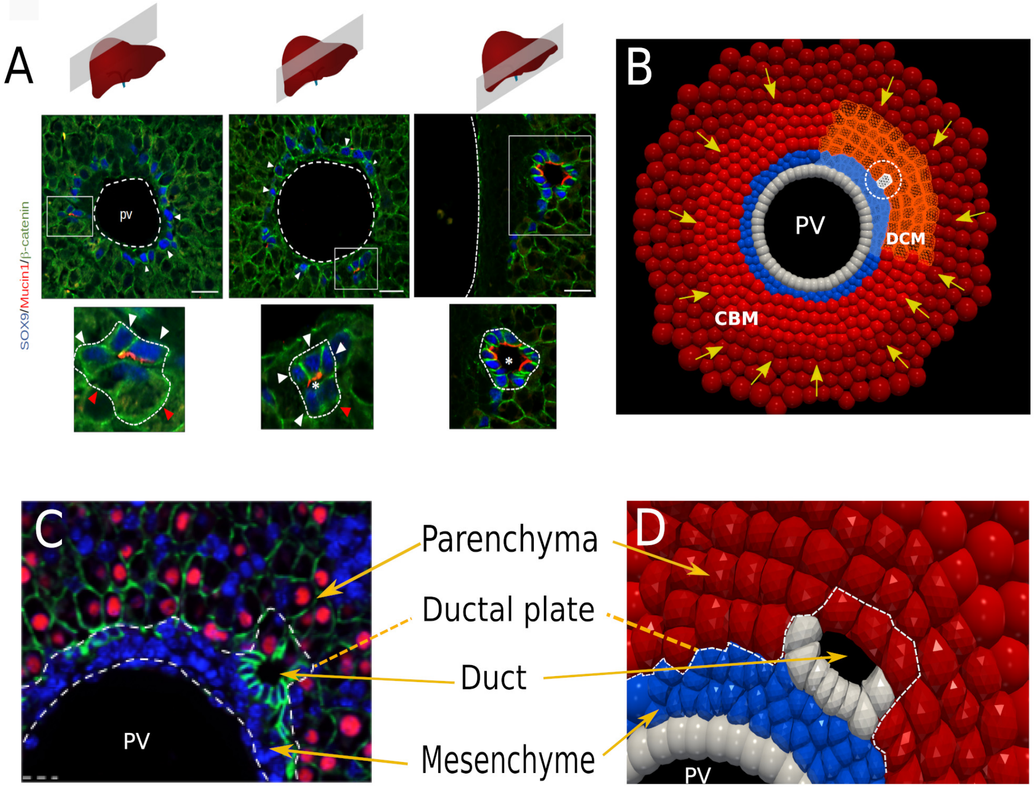

Fig 1. Experimental images and computational approach of bile duct lumen formation. (A) The bile ducts mature from the hilum to the periphery of the liver lobes, as illustrated with sections made at several distances from the hilum in mouse E18.5 liver. Nascent lumina are identified with Mucin-1 staining. White arrowheads point to SOX9-expressing cholangiocytes; red arrowheads point to hepatoblasts delineating nascent lumina. Size bar is 20 μm. (B) Snapshot of the equivalent in silico model showing the CBM and DCM regions. The initial cholangiocyte is marked by a dashed circle. The yellow arrows indicate the background pressure forces.(C) Tissular organization of the developing liver. The portal vein (PV) is delineated by an endothelium and is surrounded by mesenchyme. Cholangiocytes form a discontinuous layer of cells called ductal plate. When lumina start to form they are delineated by cholangiocytes and Hepatocyte Nuclear Factor 4 (HNF4)-expressing hepatoblasts. Epithelial cells are identified by beta-catenin staining; DAPI stains nuclei. The left panel illustrates a section through a mouse liver at embryonic day (E) 18.5; the right panel (D) shows the tissular architecture in a close-up of the in silico model.

local arrangement of cells forming the lumen, and a CBM far from the lumen-forming region (Fig 1B). We call this model the "Deformable Cell Model" (DCM). The cell surface is flexible and its shape adapts naturally to the environmental constraints.

The DCM allows coupling to CBMs, because in both models spatial displacements are based on the calculation of physical forces or mechanisms that can be represented by a physical force, as e.g. compression forces emerging from cell proliferation in a tissue. The coupling permits simulation of tissue organisation processes in a hybrid mode, where the CBM can represent cells for which a lower resolution is sufficient, while the DCM accounts for the regions where a high resolution is required [34].

Methodically, we extend the recently established model [34], that can simulate growth and proliferation in monolayers, spheroids, and regeneration after drug-induced damage in a liver lobule, by the ability of a cell to acquire a polarity defining the polar direction, and distinguish an apical and basal side. Each cell may be subject to active cortical tension and apical constriction, and can form Tight junctions (TJ) with other cells. Finally , we allow the inclusion of local osmotic effects that potentially arise in the lumen area (see Computational Models).

In this work, we have put centrally three different mechanisms that are hypothetised to contribute to lumen formation. We first investigated the individual effects of each of these mechanisms, namely: coordinated cell division, apical constriction and osmotic effects. The adaptations in our model to simulate these effects are explained in section Simulation of hypotheses). Our simulations show that each of these mechanisms can create a lumen in an idealized system without boundary conditions. In a second stage, guided by the quantification of morphological features and expression of genes in developing bile ducts specifically in embryonic mouse liver (see Materials and methods), we constructed an in silico system representing a part of the lobule containing the portal vein and surrounding tissue (Fig 1B, D). Using this architecture we have simulated the effects of the aforementioned mechanisms both individually and combined. We find that contrary to the idealized system, a coordination of these mechanisms is necessary to create an initial lumen and further lumen growth.

Materials and methods

Animals

Mice received humane care and protocols were approved by the Animal Welfare Committee of the Université catholique de Louvain. All mice (CD1 strain) were housed under a 12h light/12h dark cycle in individually ventilated cages supplied with RM3 chow (801700, Tecnilab, Someren, Netherlands), acidified water and polyvinyl chloride play tunnels. Sox9-GFP mice have been described [35].

Cell Isolation and RNA extraction

Pools of 15 livers from Sox9-GFP mice at E16.5 or E18.5 were dissected, minced and cell-dissociated in DMEM-F12 (31870-025, Gibco, Life technologies, Lederberg, Belgium) containing 1 mg/ml collagenase IV (43E14253, Worthington, New Jersey, USA), 1 mg/ml dispase (17105-041, Gibco, Life technologies) and 0.1 mg/ml of DNAse I (11284932001, Roche, Mannheim, Germany) for 30 min at 37°C. Digestion was stopped by adding an equal volume of 10% FBS in phosphate buffered saline (PBS) and cells were resuspended in 2 mM EDTA, 0.5% bovine serum albumin (BSA) in PBS and filtered on 40 µm cell strainer (087711, Fisher Scientific Merelbeke, Belgium). CD5+/CD45R+/CD11b+/7/4+/Ly-6G/C+/Ter119+ hematopoietic cells were eliminated by MACS separation using the "Lineage Cell depletion Kit" (130090858, Miltenyi Biotech Paris, France). Sox9-GFP+ cells were isolated by fluorescence-activated cell sorting (BD FACSAria III, sample and collection tubes maintained at 4°C). Total RNA was isolated using RNAqueous® Micro kit (AM1931, Invitrogen) according to manufacturer's protocol. RNA quality was evaluated using the Agilent RNA 6000 Pico Kit (Agilent Technologies) and Bioanalyzer™ (Agilent Technologies) for measuring concentration and calculation of RNA integrity number (RIN).

RNA sequencing and bioinformatics workflow

Read quality control was performed using FastQC software v0.11.7 (Babraham Institute, Cambridge, UK). Low quality reads were trimmed and adapters were removed using Trimmomatic software v0.35 (RWTH Aachen University, Germany). Reads were aligned using HISAT2 software v2.1.0 (Johns Hopkins University School of Medicine, Center for Computational Biology, Baltimore, MD, USA) on GRCm38 mouse genome. Gene counts were generated using HTSeq-count (v0.5.4p3) software and gencode.vM15.annotation.gtf annotation file and raw counts were further converted in transcripts per million (TPM).

Immunofluorescence and Imaging

Immunofluorescence stainings were performed on 6 μm sections of formalin-fixed paraffin-embedded tissues. Tissue sections were deparaffinized 3x 3 min in xylene, 3 min in 99%, 95%, 70% and 30% ethanol and deionized H2O. Antigen unmasking was performed by micro-wave heating for 10 min in 10 mM sodium citrate pH 6. Sections were permeabilized for 5 min in 0.3 % Triton X-100 PBS solution before blocking for 45 min in 0.3% milk,10 %bovine serum albumin, 0.3% Triton X-100 in PBS. Primary and secondary antibodies were diluted in blocking solution and incubated respectively at 4°C overnight and 37°C for 1 h. Pictures for immunofluorescence were taken with Cell Observer Spinning Disk (Carl Zeiss) and Zen blue software. Primary and secondary antibodies are described in Table 1.

Computational Models

Deformable Cell Model (DCM)

In the DCM used throughout this work the cell surface is discretized by a set of nodes which are connected by viscoelastic elements and interact via pairwise forces [25, 32, 34]. The nodes and their connecting elements endow a triangulation of the cell surface. The total force on each node sums up all forces on that node including mechanical forces within the cortex and external cell-cell contact interaction forces. These are combined with nodal forces originating from volume conservation, cell migration, and osmotic effects.

The dynamics of nodes is determined by an equation for each node according to Newton's law of motion, whereby inertia effects are negligible compared to friction forces, and randomness in the motion is taken into account by a stochastic active force term. For any node i of a cell[1] in which $\vec{v}_i$ denotes the velocity of node i (see Fig 2A),

---

[1] The cell index has been dropped here for clarity.

PRIMARY ANTIBODY	SPECIES	SOURCE	REFERENCE NUMBER	DILUTION
ZO-1	Rabbit	Invitrogen	61-7300	1/100
SOX9 1/250	Rabbit	Merck	Millipore	AB5535
HNF4a	Mouse (IgG2a)	R&D Systems	PP-H1415-00	1/350
Ki67	Mouse (IgG1)	BD Biosciences	556003	1/250
Mucin-1	Armenian Hamster	Invitrogen	MA5-11202	1/350
β-catenin	Mouse (IgG1)	BD Biosciences	610153	1/1000
E-Cadherin	Mouse (IgG2a)	BD Biosciences	610181	1/200

SECONDARY ANTIBODY	SPECIES	SOURCE	REFERENCE NUMBER	DILUTION
Alexa Fluor 488 anti-rabbit	Donkey	Invitrogen	A21206	1/1000
Alexa Fluor 594 anti-rabbit	Donkey	Invitrogen	A21207	1/1000
Alexa Fluor 647 anti-mouse IgG2a	Goat	Invitrogen	A21241	1/1000
Alexa Fluor 488 anti-mouse IgG1	Goat	Invitrogen	A21121	1/1000
Alexa Fluor 594 anti-armenian hamster	Goat	Jackson ImmunoResearch	127-585-160	1/1000

Table 1. Antibodies used for immunostaining.

the equation reads:

$$\underbrace{\Gamma_{ns,i}\vec{v}_i}_{\text{substrate friction}} + \underbrace{\sum_j \Gamma_{nn,ij}(\vec{v}_i - \vec{v}_j)}_{\text{node-node friction}} = \underbrace{\sum_j \vec{F}_{e,ij}}_{\text{in-plane}} + \underbrace{\sum_m \vec{F}_{m,i}}_{\text{bending}} + \underbrace{\vec{F}_{vol,i}}_{\text{volume change}}$$
$$+ \underbrace{\vec{F}_{rep,i} + \vec{F}_{adh,i}}_{\text{contact}} + \underbrace{\vec{F}_{mig,i}}_{\text{migration}} + \underbrace{\vec{F}_{osm,i}}_{\text{osmosis}}.$$

The matrix Γ_{ns} is the cell-substrate viscous friction matrix and Γ_{nn} the node-node friction matrix originating from viscous effects inside the cell or between two cells. The first and the 2nd term on the rhs represent the in-plane elastic forces and bending forces in the cortex, respectively, determined by the elastic parameters of the cortex. The third term on the rhs is a volume force controlled by the cell cytoplasm compressibility and water in/outflow. The fourth term ($\vec{F}_{adh,i}$, $\vec{F}_{rep,i}$) describe the adhesion and repulsion forces on the local surface element in presence of nearby objects as another cell. The repulsive forces herein also prevent that the cell surfaces of two interacting cells intersect. These adhesive forces are controlled by the specific adhesion energy. We assume that cell migration is un-directed and hence mimic the forces $\vec{F}_{mig}$ by a Brownian motion term with zero mean value and uncorrelated in time. The final term describes external pressure forces due to osmotic effects if these are present (for more details on the force terms, see S1 text).

Cell division is mimicked by a process in which the mother cell is replaced by a pair of daughter cells which are initially both contained by the mother cell envelope, as described in detail in ref. [34]. Basically, the two created daughter cells are initially round and separated from each other by the division plane. They grow artificially fast [2] until they reach the boundary of the mother envelope. The direction in which the cell divides can be chosen randomly (as is the case for non polarized hepatocytes) or with a preferred direction. The latter is the case when a polarized cell divides. In this case the division direction is along the polarization vector. The division plane is removed from the system after the daughter cells have found a mechanical equilibrium in this envelope. We have here slightly extended our algorithm to mimic the very short rounding-up period just before division. This is achieved by setting the equilibrium edge lengths (see S1 text) of the triangulation temporarily to a smaller value. This can cause a slight increased pressure in the cell during division.

As in the DCM cell compartments are directly represented in space and parameterized by physical quantities, the range of the model parameter values can mostly be readily be estimated (see Table 2).

New extensions to the DCM

Three major new extensions were made to permit model simulations for virtual tests of the key hypotheses of early bile duct formation. Firstly, a polarity vector for each cell was introduced, indicating the Planar Cell Polarity (PCP), and an apical-basal vector, indicating the Apical-Basal Polarity (ABP), see e.g. [36]. The polarity vector can determine in which direction a cell divides (as opposed to random division directions). The ABP vector determines the area of cell apical constriction (AC). Secondly, the model has been extended with the capability to form apical Tight Junctions (TJ) between cells. These are limited surface zones where cells strongly attach to each other (see Fig 2F). Finally, to simulate osmotic effects in the extracellular space, the concept of "Tracer Particles" (TP) has been introduced to mimic osmotic effects caused by local

---

[2] We call this a "sub-simulation" period, for which the time compared to the cell cycle is negligible.

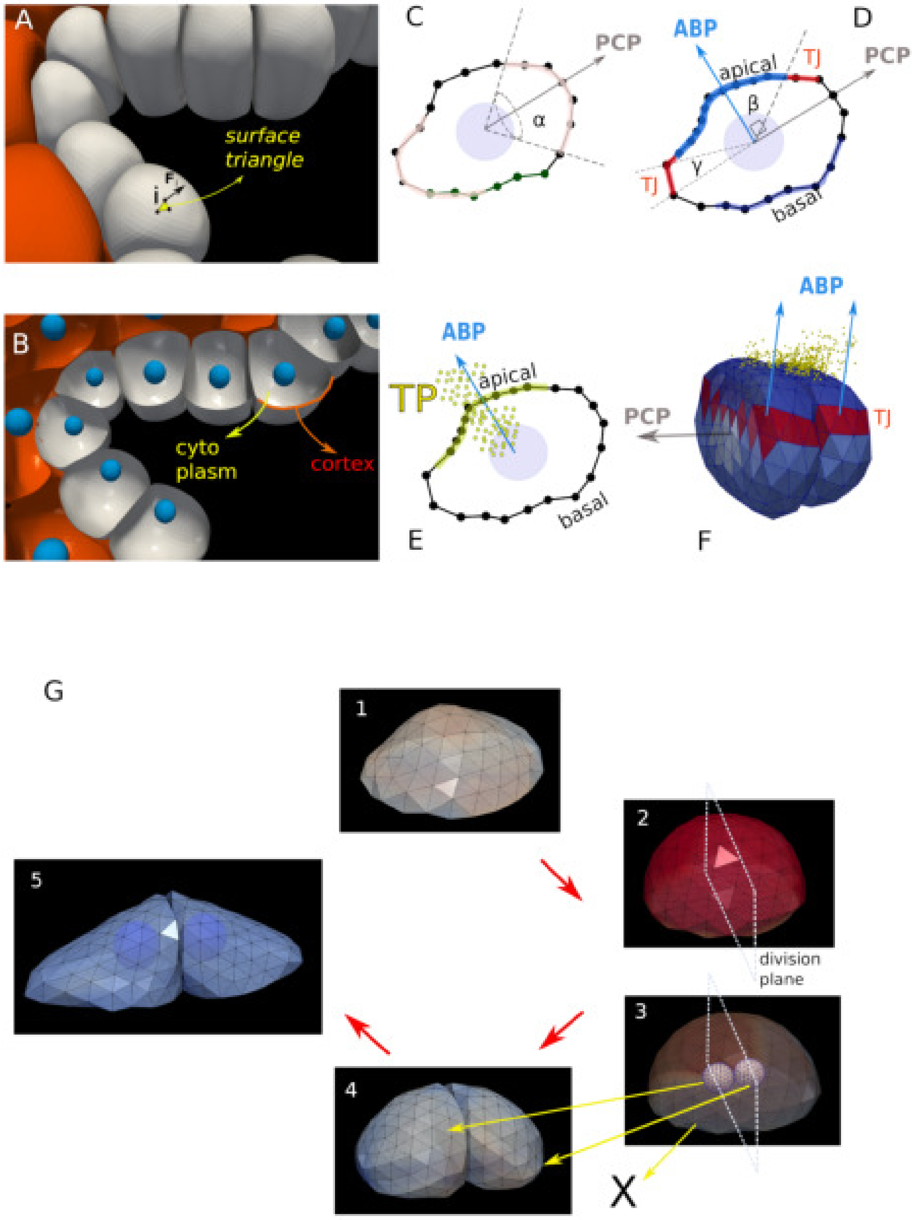

Fig 2. The DCM functional elements. A) Cell surface element (triangle) with nodal force. B) Horizontal cut section through the DCM model plane, indicating cytoplasm and cortex of the cells. C-E are cross sections through individual cells. C) Definition polarity vector (PCP) formed by a cone. Note that the zone of polarity is symmetric (light brown). D) definition Apical-Basal vector (ABP). E) Tracer Particles (TP) moving across the apical surface of the cell. F) Tight junctions between two cells in contact represented by red colored triangles. G) Overview of the different stages for the DCM cell division algorithm, extended from [34] 1: A cell with arbitrary shape. 2: just before cell division, the cell rounds up. A division plane is chosen. 3: Two new smaller cells are created on both sides of the plane inside the mother envelope. 4: The daughter cells grow artificially fast ("sub-simulation") within the mother envelope. upon confinement of the daughter cells, the mother envelope is then removed. The cells adapt to their new environment 5: Two new growing and adhering cells have been created (nuclei are shown.)

differences in salt concentration. For the technical aspects of the implementation we refer to the Supplementary Material S1 text.

The polarity vector bound to each cell can define zones of the cell surface, which are more adhesive or less adhesive (e.g. by zones with different cadherin bonds density). Here these zones are assumed to be formed by a cone centralized in the cell and aligned by the polar vector (Fig 2C). The polar surface zone on the cell is assumed to be symmetric along both cone sides, and the angle of the cone determines the surface area (as in [12, 49]).

The apical-basal vector can mark a bi-conical region where later apical constriction can occur. To mimic the constriction effect which is driven by actin-myosin contractions and whereby the apical side of the cell surface contracts, the equilibrium distance between nodes are shrinked to a shorter distance. As a consequence the nodes will move towards each other until a new mechanical equilibrium is reached. A distinction can be made in the model for "circumferential" constriction (ring-like zone where the cytoskeleton contracts) and "medioapical" constriction where the contraction is situated in the apical domain [37] (see Supplementary Material S1 text). On the opposite basal side, the cell surface remains as before, see cartoon Fig 2D. An internal structure was not needed to capture the key physics of the constriction process but could readily be added at the expense of more parameters and an increase of computational time. The latter, because explicit representation of the internal cytoskeleton would require the modeling of the cytoskeleton re-organisation during apical constriction. As the cortex is contracted on the apical side, the nodes smoothly move from the basal side to the apical side.

Tight junctions (TJ) are the areas at cell-cell contacts that have a much higher adhesion energy than the regular adhesive zones. The TJ regions are defined by the apical vector and the width of the region. The TJ is represented in the model as a conical region (belt) with a certain width controlled by an angle γ (see Fig 2D) . The belt separates apical region and basal region.

“Tracer Particles” (TP) are physical particles representing clouds of molecules that can be secreted by a cell Fig 2E . The TP can diffuse into the extracellular space without interacting with each other. They can mark the surface of a cell if they come in contact with the surface of that cell. If the particles represent salt ions, we use these marks to define the regions in the extracellular space where a net osmotic pressures on the cell surface is generated due to water attraction. Conceptually similar, TP can also represent protein concentrations that can be sensed by a nearby cell (signaling molecules). We assume in our model that tracer particles are excreted on the apical side of the cell.

Center Based Model (CBM)

The high spatial accuracy of the DCM causes longer computation times, which can limit the use of that model for large cell populations. In CBMs the individual cell shape is not represented explicitly, simplifying and approximating the results, but this comes with a significant reduction of computational time. As in the DCM, the CBM is able to mimic active migration, growth and division, and interaction with other cells or a medium. The CBM is here used to model the parts of the system that do not require knowledge of the precise cell shape. Nevertheless the CBM needs to fulfill its role as a component with a realistic boundary behavior and, if replaced by a DCM, should not lead to different simulation results. We use here the CBM to model the boundary of the portal vein (PV), which we assume not move during the time course of the simulation, and the hepatoblasts that do not participate in the bile duct formation itself, but exert a certain mechanical force to the inner cells closer to the PV (Fig 1C).

As for the DCM, the movement of cells in the CBM is mimicked by Newton’s law of

Parameter	**symbol**	**unit**	**value**	**ref**
Deformable Cell Model				
Radius Hepatoblasts	R_c	μm	$8.8 - 12$	observation, [38]
Radius Cholangiocytes	R_c	μm	$8.8 - 12$	observation, [38]
Radius Mesenchyme	R_c	μm	$8.8 - 12$	observation, [38]
Cycle time*	τ	h	24	[38]
Cortex Young's modulus	E_{cor}	Pa	1000	[39]
Cortex thickness	h_{cor}	nm	500	observation
Cortex Poisson ratio	ν_{cor}	-	0.5	[40]
Cell bulk modulus	K_V	Pa	$750 - 2500$	[38], [40]
Cell-cell adhesion energy	W	J/m^2	$10^{-5} - 5 \cdot 10^{-5}$	[38],CR
Nodal friction	γ_{int}	Ns/m^3	$1 \cdot 10^{-4}$	CR
Cell-cell friction	γ_{ext}	Ns/m^3	$5 \cdot 10^{10}$	[41, 42],CR
Cell-ECM friction	γ_{ECM}	Ns/m^3	10^8	[41],CR
Cell-liquid friction	γ_{liq}	Ns/m^3	500	CR
Motility	D	m^2/s	10^{-16}	[38, 44]
Center Based Model				
Young's modulus*	E	Pa	450	[38]
Poisson's modulus	ν	$-$	0.47	[38]
Motility	D	m^2/s	10^{-16}	[38, 44]
Lobule				
Radius portal veins	R_{pv}	μm	50	[38]
Pressure lumen ducts	P_L	Pa	$0 - 100$	CR
Pressure tissue	P_b	Pa	50	PC

Table 2. Nominal physical parameter values for the model. An (*) denotes parameter variability meaning that the individual cell parameters are picked from a Gaussian distribution with ±10% on their mean value. CR : Calibration Runs. Unless indicated, the cell parameters for the CBM and DCM are identical. PC : Personal communication.

motion. Different from the DCM, where all forces on a large set of nodes characterizing cell shape has been considered, in the CBM only forces on the center of mass of the cell is taken into account. The center of mass position of each cell i is obtained from a Langevin equation of motion, which summarizes all forces on that cell including a force term mimicking its micro-motility:

$$\Gamma_{ECM}\vec{v_i} + \Gamma_{c,cap}\vec{v_i} + \sum_j \Gamma_{cc}(\vec{v_i} - \vec{v_j}) = \sum_j \vec{F}_{cc,ij} + \vec{F}_{mig,i} \tag{1}$$

The lhs. describes cell-matrix friction, cell-capsule friction and cell-cell friction, respectively. Accordingly, Γ_{ECM}, $\Gamma_{c,cap}$, and Γ_{cc} denote the friction tensors for cell-ECM, cell-capsule-, and cell-cell friction. The first term on the rhs. of the equation of motion represents the cell-cell repulsive and adhesive forces $\vec{F}_{cc}$, the 2nd term is an active force term $\vec{F}_{mig}$, mimicking the cell micro-motility. $\vec{F}_{mig}$ is mimicked by a Brownian motion term with zero mean value and uncorrelated in time (more details can be found in the Appendix).

Different from DCMs, the CBM geometric bodies may substantially overlap each other in contact. The total cell-cell interaction force $\vec{F}_{cc}$ for small overlaps can be approximated by the Johnson-Kendall-Roberts - force [45] that in absence of adhesion reduces to the well-known Herzian contact force:

$$F_{rep,ij} = 4/3 E_{ij}\sqrt{R_{ij}}\delta_{ij}^{3/2}, \tag{2}$$

in which E_{ij} and R_{ij} are defined as

$$E_{ij} = \left(\frac{1-\nu_i^2}{E_i} + \frac{1-\nu_j^2}{E_j}\right)^{-1} \text{ and } R_{ij} = \left(\frac{1}{R_i} + \frac{1}{R_j}\right)^{-1},$$

with E_i and E_j being the cell Young's moduli, ν_i and ν_j the Poisson numbers and R_i and R_j the radii of the cells i and j , respectively. $\delta_{ij} = R_j + R_i - d_{ij}$ denotes the overlap of the two un-deformed spheres, whereby $d_{ij} = ||\vec{r}_j - \vec{r}_i||$ is the distance of the centers of cells i and j.

However, it is well-known that the original Hertz contact model becomes inaccurate in systems with large cell densities, where it underestimates the contact forces and becomes inconsistent with the forces in the DCM [43]. To still enforce consistency with the by construction more accurate DCM that accounts for multi-body interactions, the Young modulus for every cell E_i in the Hertz model was replaced by an "apparent" contact stiffness $\tilde{E}_i$ that increases as function of the local cell density. The increase in local cell density is approximated by the average cell-to-cell distance $\tilde{d}_i =< 1 - d_{ij}/(R_{ref,i} + R_{ref,j}) >$. The new apparent Young modulus is computed by

$$\tilde{E}_i = E_i + a_0\tilde{d}_i + a_1\tilde{d}_i^2 + a_3\tilde{d}_i^3$$

The modification of the Hertz contact force model was calibrated with DCM using the calibration procedure introduced in ref. [34]. As a consequence, as long as cell shape does not largely deviate from a sphere CBM and DCM generate statistically equivalent simulation results hence can be used in a hybrid model by switching between them if necessary (see [34] for details). Using this hybrid model permitted a significant reduction in computation time.

Results

Morphological features of cells during biliary lumenogenesis

First, the experimental observations are presented that support alternative hypotheses on the mechanisms controlling early lumen formation during duct development. In a second step the three different hypotheses studied throughout this work are derived.

At the onset of biliary lumen formation, cholangiocytes are located adjacent to the periportal mesenchyme, which separates the cholangiocytes from the endothelial cells lining the portal vein. The parenchyma is predominantly composed of beta-catenin-positive hepatoblasts, hematopoietic cells and vascular spaces (Fig 1A) [46]. Beta-catenin is here used as epithelial marker.

Lumen formation was shown to be initiated at single cholangiocytes expressing Na+/H+ exchanger regulatory factor 1 (NHERF1) and Moesin at their apical pole [7]. Fig 1B extends this information by illustrating the expression of Mucin1 (MUC1), a cell surface glycoprotein, at the apical pole of cholangiocytes. Initially, a single cholangiocyte, identified by expression of the biliary marker SRY-related HMG box transcription factor 9 (SOX9) expresses Mucin-1 (MUC1). The expression of MUC1 then spreads to adjacent cholangiocytes, in parallel with expansion of the lumen and differentiation of hepatoblasts into cholangiocytes. The various steps of lumen formation are shown in Fig 1B at embryonic day (E18.5) within the same liver. This is made possible because duct formation progresses from the liver hilum to the periphery of the lobes, with more mature structures being located near the hilum and less mature structures more peripheral in the liver.

Lumen formation is associated with apico-basal polarization of the cholangiocytes. This is well illustrated by expression of NHERF1, Moesin, MUC1 and osteopontin, all at the apical pole of the cholangiocytes (refs. [4, 7] and Fig 1B). Further, when determining the presence of tight junctions between cells delineating a developing lumen, we found that the tight junction marker Zonula Occludens 1 (ZO1) is detectable at the junction between adjacent cholangiocytes and between a cholangiocyte and a hepatoblast in asymmetrical ductal structures (Fig 3A). In contrast, adjacent hepatoblasts delineating a developing duct lumen do not yet express detectable ZO1 near the biliary lumen, indicating that tight junction formation parallels maturation of the hepatoblasts to cholangiocytes.

Hypothesis I: differential proliferation rates: Since the portal vein is surrounded by a double layer consisting of an inner cholangiocyte and an outer hepatoblast cell layer, differential proliferation rates within the two distinct layers may create buckling forces large enough to rupture the contacts between the two layers leading to generation of a lumen. Therefore, we measured the percentage of proliferating cholangiocytes and hepatoblasts. Using SOX9/Ki67 and HNF4/Ki67 co-stainings we found that 26.0% of SOX9-positive cholangiocytes and 10.7% of HNF4-positive hepatoblasts were proliferating at E16.5 (Fig. 3B) (n = 3 livers; 630 cholangiocytes and 549 hepatoblasts were analyzed). The first hypothesis studied below by the computational model is that this difference may be responsible to a lumen formation.

Hypothesis II: apical constriction: Formation of a lumen in a cylindrical duct implies that the apical pole of the cells aligning the lumen is (geometrically) shorter than the opposite basal pole. We verified that this was the case. We measured the length of the apical and basal poles of cells involved in the formation of asymmetrical ductal structures (Fig 3C). Apical shortening was obvious in cholangiocytes, despite significant cell-to-cell variability. The heterogeneous morphology and circumferential expression of E-cadherin in hepatoblasts did not allow to delineate their apical and basal

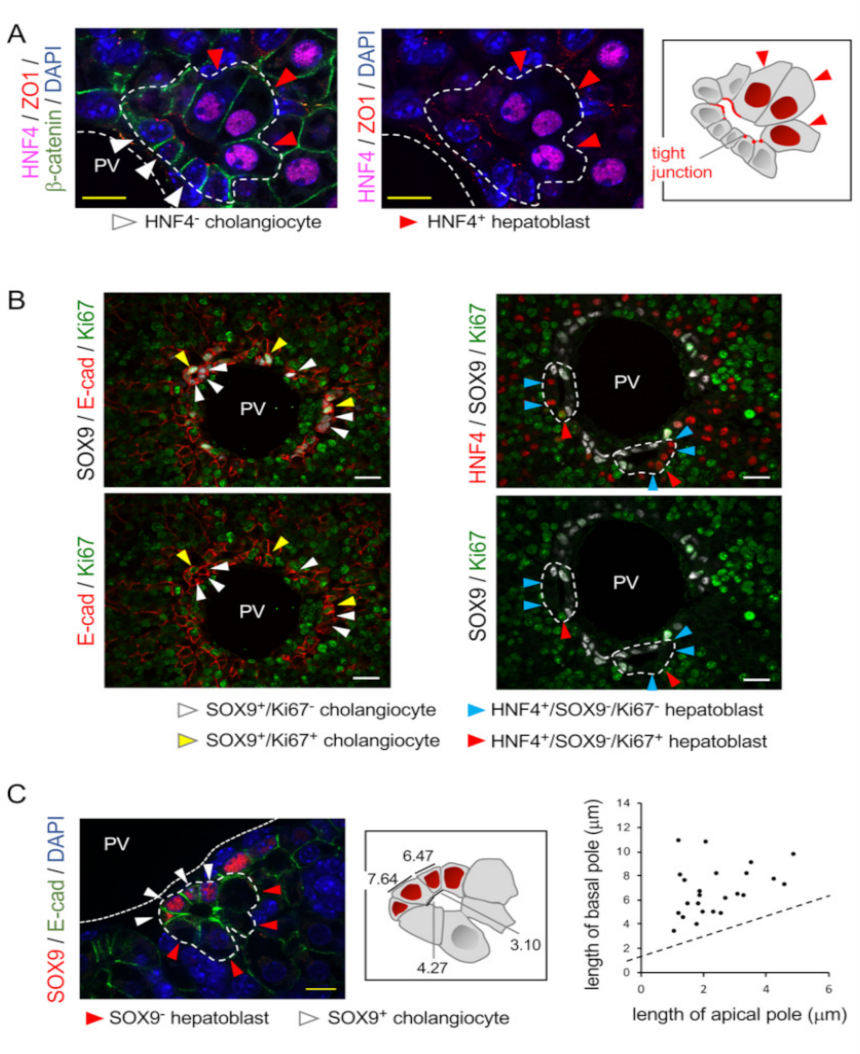

Fig 3. Morphological features of cells delineating developing biliary lumen. (A) Tight junctions are detected between HNF4- cholangiocytes and between cholangiocytes and HNF4+ hepatoblasts; but not between adjacent hepatoblasts. (B) Proliferating SOX9+ cholangiocytes and HNF4+ hepatoblasts are detected by Ki67-staining in E16.5 embryonic livers. E-cad: E-cadherin. (C) Apical constriction in cholangiocytes. Developing ducts are delineated by white dotted lines. White size bar, 20 micrometer; yellow size bar 10 micrometer. PV: portal vein

sides and measure their lengths in hepatoblasts. However, plotting the length of the apical sides as a function of the length of the basal sides in cholangiocytes showed that all cells display apical constriction, the ratio of basal/apical length being < 1. Therefore, apical constriction whereby the apical shortening is driven by an active constriction of the apical side of the cell, would be a candidate mechanism for the lumen formation.

Hypothesis III: osmosis-driven lumen formation: The accumulation of fluid may be a potential driving force for lumenogenesis. Such accumulation of fluid is expected to result from osmotic changes and water transport, which depend on ion transporters and water channels. To verify if ion transporters and aquaporins were expressed at the onset of lumenogenesis, we purified the cholangiocytes at E16.5 and E18.5. Embryonic livers from SOX9-GFP embryos were dissociated; hematopoietic cells were removed by magnetic cell sorting, and GFP+ cells were FACS-purified. Total RNA was extracted and subjected to RNA sequencing. Expression of apical Aquaporins 1 and 8, Multidrug resistance 1 P-glycoprotein (Abcb1/Mdr1), Na+-independent Cl−/HCO3− exchanger (Slc4a2/Ae2), Cystic fibrosis transmembrane regulator (Cftr) and Na+-HCO3− cotransporter (Slc4a4/Nbc1) [47, 48] was already detected at E16.5, indicating that regulators of ion and water transport were present at the onset of lumenogenesis (Fig 4). Hence osmosis is another candidate for the lumen formation. In intrahepatic bile ducts, regulated and inducible water influx creates unidirectional advection.

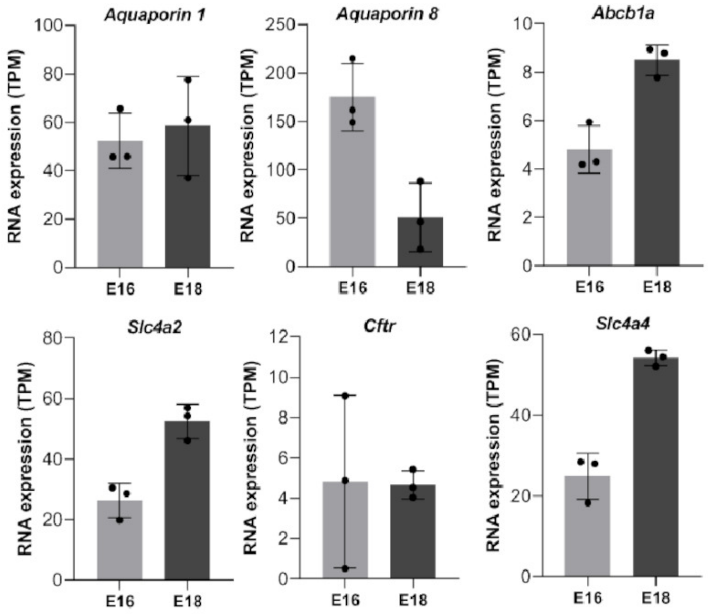

Fig 4. Expression of ion transporters and water channels during biliary lumenogenesis. Expression of ion transporters and aquaporins was measured by RNA sequencing of total RNA extracted from purified developing cholangiocytes.

In summary, we identified three candidate mechanisms possibly driving bile duct formation, each of them being compatible with experimental observations: (1) Differential proliferation rates within the cholangiocyte and hepatoblast cell layer within the double layer aligning the portal vein. (2) Apical constriction in at least one of the two cell layers. (3) Secretion of water by osmosis if the salt concentration at the two-layer interface is locally elevated, and fluid leakage is restricted by tight junctions. However, the double layer is constrained from the side of the cholangiocyte layer by mesenchyme enclosing the lumen of the portal vein and from the side of the hepatoblast layer by a largely unstructured mass of proliferating hepatoblasts, blood vessels and hematopoietic cells that may exert mechanical compressive stress on the double layer and hence counteract lumen formation. The balance of arising forces, proliferating forces, bending forces, deformation and contraction forces, is impossible to estimate by reasoning alone. Hence we implemented a representative tissue section within a computational ABM and simulated each of the three hypothesized mechanisms to explore whether any of the three hypotheses would have to be excluded based on physical interactions. This is possible as the computational model is parameterized by measurable parameters, for which the ranges are largely known.

In a next step we tested whether each of the three candidate mechanisms is able to generate a lumen in an idealized layer before embedding the bi-layer into its natural environment during bile duct formation.

Computational model: Each mechanism is able to generate a lumen in an isolated double layer

To illustrate the effect of differential proliferation, apical constriction and osmotic forces, we first considered a minimal, idealized subsystem of two layers of each 10 cells which adhere to each other (Fig 5). The system is assumed to be embedded in a fluid medium without external resistance from other cells or ECM. Simulations with this system can help us to understand the effects of these mechanisms in absence of effects from surrounding cells.

Mechanism I: Creation of a lumen by pure cell division

Cell proliferation can introduce a buckling instability in epithelial sheets and formation of cavities (see e.g. [49, 50]). We illustrate this with a simulation of our reduced system. Four cells in the upper layer are selected, able to proliferate. All other cells remain quiescent. Furthermore, only these 4 cells are assumed to be polarized. The polarization direction is here uniquely determined by the mutual adhesive contact regions between the cells (identified by triangles of the cell surface) between a cell-cell contact of the same type (red marks in Fig 5A-1) [51]. Thus, for each of these cells the polarization vector is initially parallel to the layer, but can change and is updated along with the relative positions of the cells. In addition, an apical side and basal side are introduced (determined by an apical vector, which is perpendicular to the polar vector). The apical side is oriented towards the other cell layer, while the basal side is oriented outwards. Two cases are now distinguished: (i) When cell division occurs, the division direction is always along the polar vector (Fig 5A-1). Moreover, the polar contact area is assumed to be populated with a higher intercellular density of molecular complexes forming tight junctions and thus higher in adhesion energy, compared to the average cell adhesion energy. Contrary, the apical side area has almost no cadherins.

(ii) The cells are still assumed to be polarized, but this polarization has no effect on the intercellular distribution of adhesive contacts, nor on the orientation of proliferation, which is here chosen to be random corresponding to a uniform distribution Fig 5A-2).

For both cases we assume that only for of the lowaer cells can proliferate without any restriction (division time 24h). For the case (i) the formation of a convexly shaped lumen after a few cell divisions occurs (Fig 5A-1 and SI : Video 1). The convex shape of the lumen is conserved even after several cell divisions but eventually, new buckling effects will arise. Contrary, case (ii) does not result in a clear single lumen formation, as cells basically move in random directions due to the proliferation, thereby filling up any previously formed cavity (see Fig 5A-2 and SI : Video 2). This shows the importance of both cell polarity and polar division in the lumen creation, consistent with the findings in ref. [52].

Mechanism II: Creation of a lumen by apical constriction.

During apical constriction, the surface area of the apical side shrinks due to a local contractile effect of the cortical cytoskeleton. When this effect takes place on several

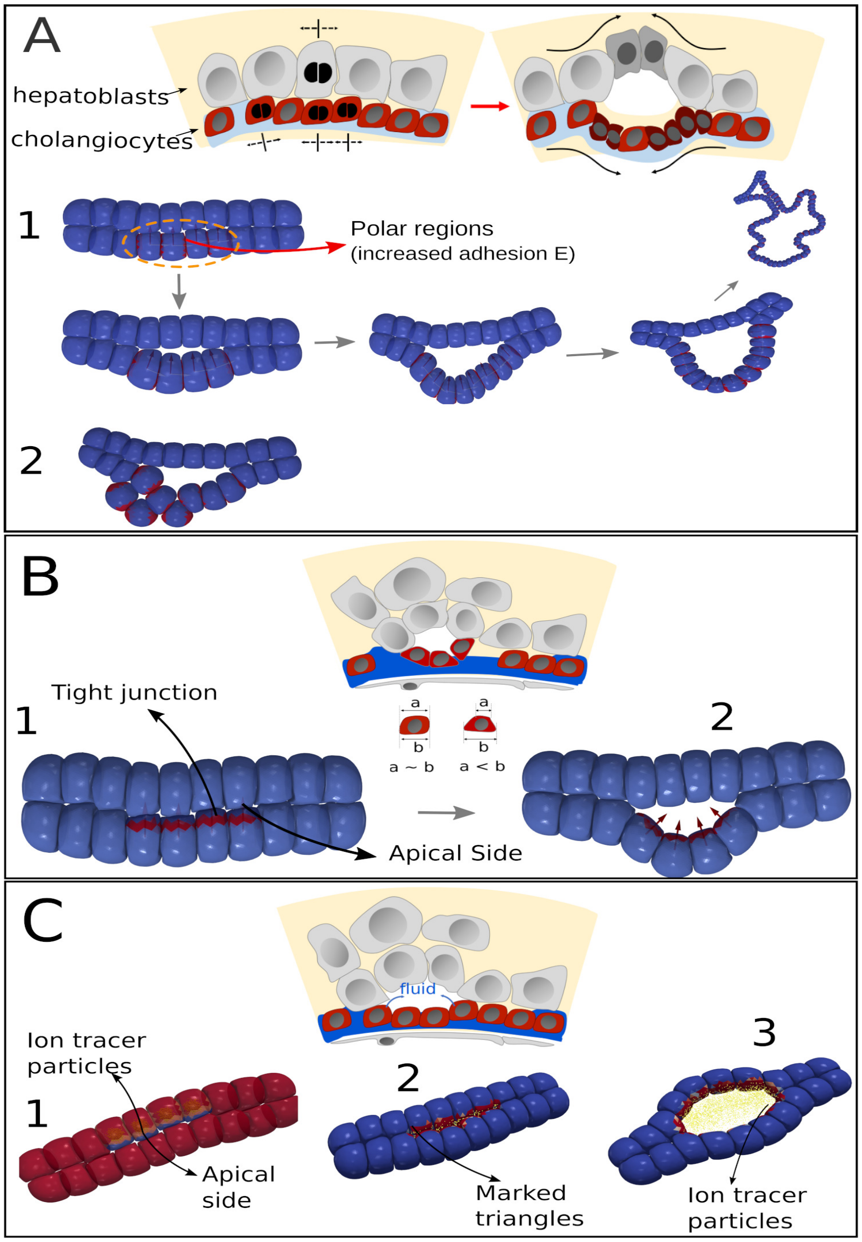

Fig 5. Possible mechanisms of lumen formation. A) Cell division. 1: double layer of cells with 4 dividing cells (indicated by orange dashed line). Cell division goes along PCP polarization. 2: random directed cell division. 2) Apical constriction. 3) Osmosis in extracellular space.

adhering cells simultaneously, a new mechanical equilibrium emerges, driving the layer to bend outwards. Apical constriction has been modeled using vertex models showing that it can significantly contribute to tissue distortion [53–55], and by center-based models to explain gastrulation in sea urchin [49]. Here, we further assume that along with apical constriction, also Tight Junctions (TJ) are present. TJ involve adherent junctions which are usually localized at the apico-lateral borders of epithelial cells [56].

In the minimal system, first the apical vectors of the four upper cells are defined.

These point towards the underlying cell layer (red arrows in Fig 5B). The apical vectors define the cone of the apical region in those cells (Fig 5B-1, dark blue regions). These regions have a smaller adhesion energy than the rest of the cell surface. On the contrary the tight junction regions (red triangles in Fig 5B) have a higher adhesion energy value. At the moment at which a strong constriction is applied in the apical region a small cavity is forming. No cell division is involved. We note here that when packed in a sheet such as this is the case for the four central cells, the DCM simulations show some wedge-like cell shapes (see Fig 5B-2 and SI : Video 3) as often depicted in textbooks. Altogether, these simulations show that apical constriction of cells can indeed create a small initial cavity.

Mechanism III: Creation of a lumen by osmotic effects induced by ions.

As previously explained, regulators of ion and water transport could be identified in the apicial side of cholangiocytes at the onset of lumenogenesis. This machinery permits either generating differences in the mole fraction of solutes between cell and extracellular cavities, resulting in osmotic pressure-driven water flow or osmotic pressure-driven water flow as a consequence of already existing differences in solutes in intra-and extracellular space, in both cases, until the sum of hydrostatic and osmotic pressures in the cavity and outside of it are balanced. The excretion of ions or salts subsequently dissociating into ions and their diffusion process in the computational model is mimicked by “tracer particles” (TP). In the simulation we assume that the four cells are now able to secrete ions (TPs) through a specific region of the cell area (Fig 5C-3). In agreement with the experiments the “permeable” region is the apical side of the cells, which in turn is determined by the cell apical-basal vector. As in the previous case, this vector points towards the other cell layer. Right after the simulation has started the tracer particles are created in the cell center and diffuse inside the cells. They gradually move towards the cell boundary and can cross the cell membrane on the apical side where there is free extracellular space mimicking the effect of ion transporters generating an osmotic effects (Fig 5C-2). The osmotic pressure difference -assumed to be constant here for simplicity- triggers water inflow into the initially small extracellular cavity. The in flowing water exerts a hydrostatic pressure on the cell walls delineating the cavity (marked by red triangles in Fig 5C-2)) and pushed them away hence increasing the cavity volume. Whether cells from the one layer will be separated from those of the other layer, depends on the magnitude of the pressure forces as well as on the surface adhesion energy of the cells. In Fig 5C-3 the case is shown where the cell-cell adhesion energy between the two cell layers at the apical side is relatively small compared to the osmotic energy.

As a consequence, the cell layer separates from the other layer and a cavity is formed that keeps on growing (see also SI : Video 4). When the osmotic pressure is finally equilibrated with the tensile adhesive stress between the cells, the lumen stops growing. However, if the osmotic forces were too large, the lumen would eventually burst. Here the presence of tight junctions between the cells helps preventing this to occur as they reinforce the cell-cell adhesion and thus provide a larger mechanical resistance to osmotic forces. Moreover, the tight junctions prevent ions to move in between cell-cell boundaries thereby hindering leakage out of the formed cavity. The latter phenomenon can only be modeled approximately at this chosen resolution of the model but by choosing a higher resolution, this would become possible, see section Discussion and Conclusions).

Model: Simulation of lumen formation in bile duct system

In the previous section it has been shown by computational modeling that initial lumen formation can be independently induced by each of the different three different hypothesised mechanisms in an idealized system with no external constraints to the system of cells. In the next step it is studied whether these mechanisms are able to cause lumen formation if surrounded by tissue, which is the situation in bile duct development in the developing embryo. In addition, as it is observed that hepatoblasts aligning the emerging lumen are gradually replaced by cholangiocytes, the combined effects of "non-mechanical" cues such as cell cycle progression and cell signaling has to be taken into account. The pursued modeling strategy is to identify the minimal set of mechanisms that are able to cause lumen formation, starting from the time point where no lumen is present (few or no cholangiocytes) until a full lumen completely surrounded by cholangiocytes has been established (see Fig1).

Configuration of the in-silico embryonic liver system

Bile duct formation is guided by a complex interplay of cell signaling and cell mechanics, resulting in initial lumen formation, the formation of tubular branches, and possibly merging of those branches [2]. Simulating this entire development would require a full 3D simulation demanding large computational power and additional three-dimensional experimental data. Here the focus is on the initial stage of formation of a single bile duct. This can be mimicked by simulation of the tissue organisation dynamics in a 2D cut of the portal vein area chosen such that the forming lumen lies in the simulated cut section. In the simulations this is warranted by constraining the cell motion within a plane created by a transversal cut of the portal vein, noticing that the bile ducts develop parallel to the portal veins later forming the portal triads. This chosen model configuration is representative to the configuration in the experimental images.

In order to cope with the higher computation time of the DCM, a hybrid model of DCM and CBM has been constructed in which the DCM and CBM cells interact in a mechanically consistent way [34]. The cells initially are labeled as either being endothelial cells, hepatoblasts (and hematopoietic cells), or mesenchyme cells. The mesenchyme and the hepatoblasts in the active segment localized closest to the mesenchyme are represented by DCM, the hepatoblasts further away from the portal vein are represented by CBM. The latter cells are assumed to not directly participate in the bile duct formation. This turned out to be a self-consistent assumption in that during the simulations no re-arrangements of cells occurred that resulted in direct interactions of CBM cells and DCM cells aligning the emerging lumina. The portal vein endothelial cells are represented by CBM cells fixed in space. The ECM present in intercellular space was not explicitly modeled. However, as in ref. [34], ECM-cell friction has been considered at those surface regions of each cell that are not in direct contact with other cells.

In the experimental images the cholangiocytes appear to be significantly smaller than the surrounding hepatoblasts. Their cell surface ratios (extrapolated from the circumference) varied of up to a factor of 2 to 4 (Fig 6). The size difference of hepatoblasts to cholangiocytes may be attribute to three main causes: (i) cholangiocytes are likely responsible for excreting salts into the luminal space through the apical side, thereby attracting water. This water content may be partially withdrawn from the cholangiocytes themselves (i-a). On the other hand, aquaporins are also present on the basal side (i-b). The cholangiocytes seem thus rather to act as a "pump", withdrawing water from regions further away from the bile duct. (ii) Cholangiocytes being neighbors to hepatoblasts may instantly look smaller because they are likely the differentiated daughter cells of a former hepatoblast. Indeed, it was observed that some hepatoblasts adjacent to a cholangiocyte still have a large size but start expressing some cholangiocyte proteins (SOX9+). Upon cell division, they may become cholangiocytes expressing high levels of SOX9+. Hence, we may also assume that cholangiocytes induce active hepatoblast-to- cholangiocyte transformation. (iii) The volume of a mature cholangiocyte is inherently smaller than that of a hepatoblast. This also means that after a hepatoblast divides, the two daughter cholangiocytes have a volume that is relatively large compared to a mature cholangiocyte. As a consequence, the criterion for cell division, i.e. doubling of the initial volume, will be reached relatively quickly and a new cell division will take place shortly after the first cell division. This results in cholangiocytes, which are significantly smaller than the original hepatoblasts.

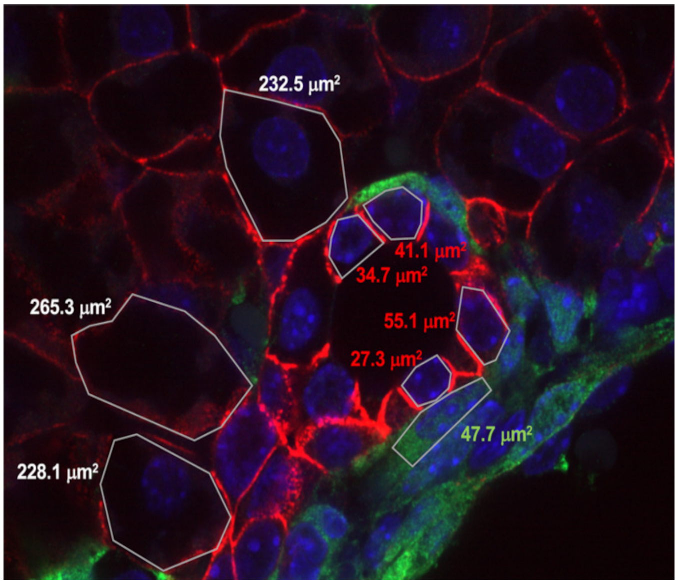

Fig 6. Detail image of the lumen with indicated cell surface areas. White numbering: hepatoblasts, red numbering: cholangiocytes, green numbering: mensenchyme. The picture is from an E18 mouse liver expressing eYFP in the mesenchyme. Red membrane staining of hepatoblasts and cholangiocytes: E-cadherin; green staining of mesenchyme: eYFP.

The hypotheses i-b), ii) and iii) have been adopted in our model. However, it is not excluded that hypothesis i-a) is also valid, solely or in combination with i-b). The former could be tested in more depth by adding an extra equation for the change in cell reference volume (see Eq.8) that describes how much water a cholangiocyte net loses during and after its differentiation. However, in the scope of this paper this option has been ignored. Because of hypothesis iii), an initially fast appearance of several new cholangiocytes may occur (Fig 1A). This seems to be in agreement with the experimentally observed configuration (Fig 3A), where 4 adjacent cholangiocytes in a row are observed, while the other (bigger) cells are still merely hepatoblast.

The cells are initially configured as shown in Fig 1C. The initial size of all the cells is randomly sampled from a Gaussian distribution with average size $d_{mes} = 10\,\mu\text{m} \pm 10\%$ for the mesenchymal cells, $d_{hep} = 15\,\mu\text{m} \pm 10\%$ for the hepatoblasts. The following Boundary Conditions (BC) have been applied: on the outer circumferential side the tissue is allowed to expand due to cell growth, yet a constant “background” pressure P_b is exerted on to the outer hepatoblasts in radial directions towards the portal vein, mimicking the mechanical resistance of the surrounding tissue (see Fig 1). The reference value was set to $P_b = 50$ Pa (personal communication), which is of the same order of magnitude as the elastic modulus of liver matrix ([57]). On the inner boundary, the fixed endothelial cells (CBM) prevent cells from moving toward the portal vein. More details and technical aspects about the BC are given in the Appendix. An animation can be viewed in SI : Video 5.

The simulations start with the assumption that a lumen originates from a single hepatoblast located in the middle of a segment (Fig 1). At a certain point in time, a differentiation of this hepatoblast into a cholangiocyte is induced, likely mediated by contacts between portal vein-associated mesenchymal cells and adjacent hepatoblasts. The new cholangiocyte undergoes cell cycle progression. The initial size of the cholangiocyte is set to 0.75 times the size of a hepatoblast. The cholangiocyte is assumed to have acquired an apical direction pointing away from the portal vein centre and hence a polar direction perpendicular to the apical direction [36]. After some time, the cholangiocyte divides, creating two daughter cells. These two adherent daughter cholangiocytes are initially proliferating and also become immediately polarized with the same polarity as the mother cell.

We recall that about 20% of the cholangiocytes nearest to the portal vein are proliferating (Ki67+ staining) in the stage E16.5 to E18.5. This is in contrast to the hepatoblasts of which only 11% proliferate. Similar behavior was observed in ref. [58]. As information about the exact mechanisms maintaining these proliferation rates was lacking, an algorithm was implemented enforcing the experimentally observed rates. The algorithm keeps track of the number of proliferating cells for each cell type, and randomly picks cells that become quiescent if the observed number of proliferation in the simulation exceeds the experimentally observed number (see Supplementary Material S1 text).

Simulation of hypotheses

In this section the simulation results applying the hypotheses introduced above in the context of the tissue of the developing embryo (section Computational model: Each mechanism is able to generate a lumen in an isolated double layer) are presented. The complexity of the model is stepwise increased, and the simulated lumen shapes and sizes are compared to the experimentally observed ones. All simulations run for 24 hours after the time point the first cholangiocyte appeared. This initial cholangiocyte get polarized. The basal membrane of the cholangiocyte is oriented towards the mesenchyme (1A), while the apical vector points away from the PV centre, and the polar vector is aligned with the portal vein (PV) tangent. This can be induced by depostion of laminins in the ECM surrounding the portal vein [59] The division orientation is thus oriented along parallel to the PV, as depicted in (Fig 7)A. Notch-like signaling from cholangiocytes to adjacent hepatoblasts is possible, meaning that a hepatoblast can differentiate into a cholangiocyte subject to the conditions that they are in contact to each other, and that the hepatoblast borders on a free extracellular space. The cholangiocyte will try to orient its apical vector to the free extracellular spade The signaling is controlled by a single time parameter T_N. We assume that $T_N > 0$ as otherwise the hepatoblasts transform immediately to cholangiocytes, which is in contrast with the gradual expression of SOX9 observed in 3C. Here, we postulate that $T_N = 2h$. However, the effect of T_N will be further shown below. For each model and the same parameter set, the results were averaged over 5 simulation runs to incorporate random effects.

The models discussed hereafter include one or several components more than the reference scenario defined as "Model 0", where the initial daughter cholangiocytes proliferate further into random directions. Apical constriction is not present and osmotic effects are negligible. The results of the simulation with model 0 show a growth in which few hepatoblasts develop to cholangiocytes, without any cavity formation and lumen growth assuring that no lumen forms in absence of the three hypothesised mechanisms (Fig 7)B.

Model 1:

In model 1 the cholangiocytes get polarized and the division orientation is oriented along the PCP vector. Both cholangiocyte daughter cells inherit the polarization direction of the mother cell right after cell division. The results with model 1 indicate now the creation of a small cavity, but without clear and stable lumen growth over time (Fig 7D) as the cavity surface remains smaller that the cross sectional surface of one cell. This is in contrast to the findings of mechanism I (section Model: Testing of three basic mechanisms). The difference can be attributed to the fact that in model 1 the surrounding cells are exerting a pressure preventing a further growth of the cavity.

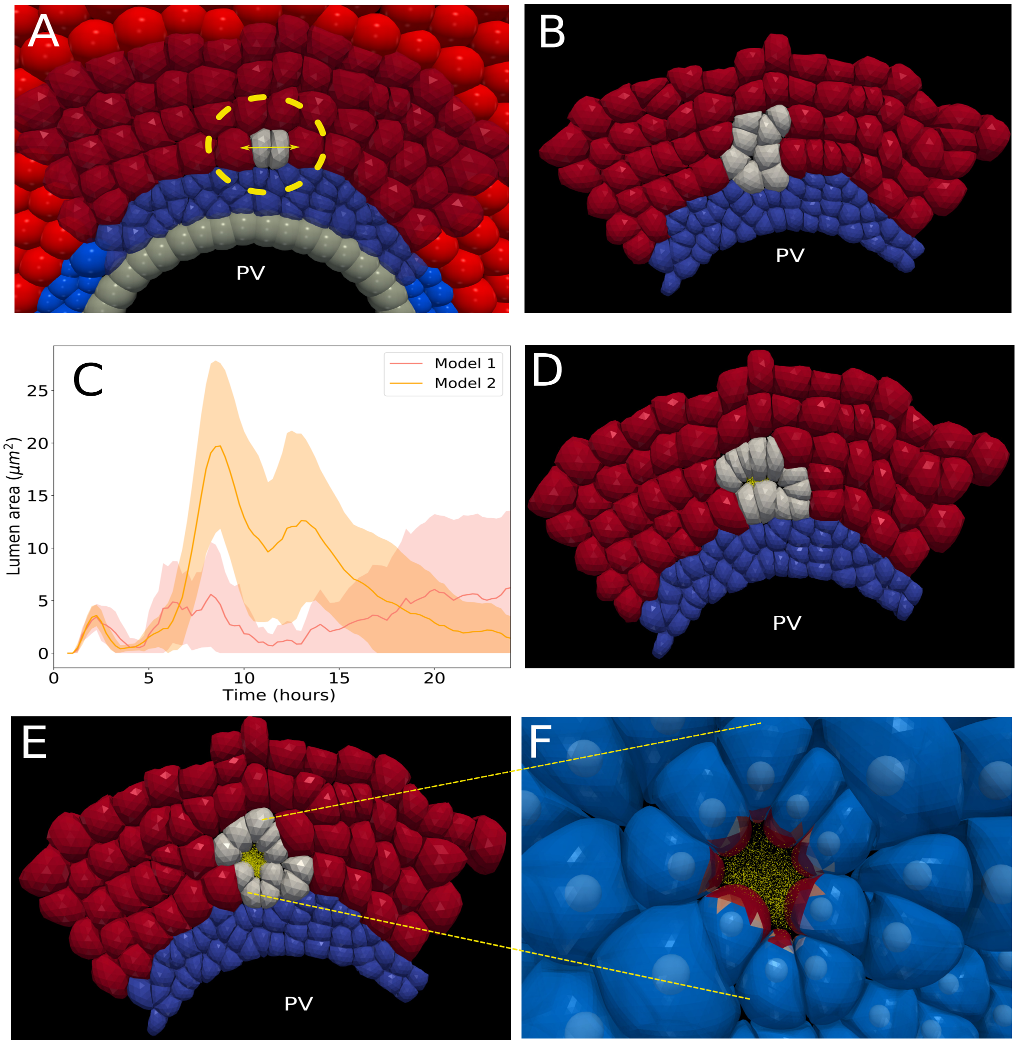

Fig 7. Simulation results for Model 1 and Model 2. A) just after initial state, where a cholangiocyte divides in two daughter cells. The division direction is indicated by the arrow. B: Snapshot of a simulation for Model 0 ($t = 12$). C) lumen area versus time for model 1 and model 2, for different runs (no osmotic effects present). D) Snapshot of a simulation for Model 1 ($t = 12$). E) Snapshot of a simulation for Model 2 ($t = 12$). The red, grey and blue cells indicate hepatocytes, cholangiocytes and the mesenchyme respectively. F: simulation snapshots for model 2 showing tracer particles (yellow) and apical sites of the cholangiocytes (red).

Model 2: We extend model 1 with the capacity of the cholangiocytes to perform apical constriction of the apical side. This involves a ring-like zone of strong constriction with the tight junctions, and a weaker constriction of the apical domain (see S1 text for details). All other mechanisms are the same as in model 1. Compared to the runs of Model 1, we find an initial stronger signal for cavity area, due to the retraction of the apical domain caused by the mechanical forces of apical constriction. However, this signal is not maintained as it weakens after after $t = 12h$ and becomes similar to Model 1 after 24h, see Fig 7C. The reason is that despite the shape formation, the increasing compression due to cell division in combination with the pressure exerted by the surrounding tissue does not permit formation of a stable cavity.

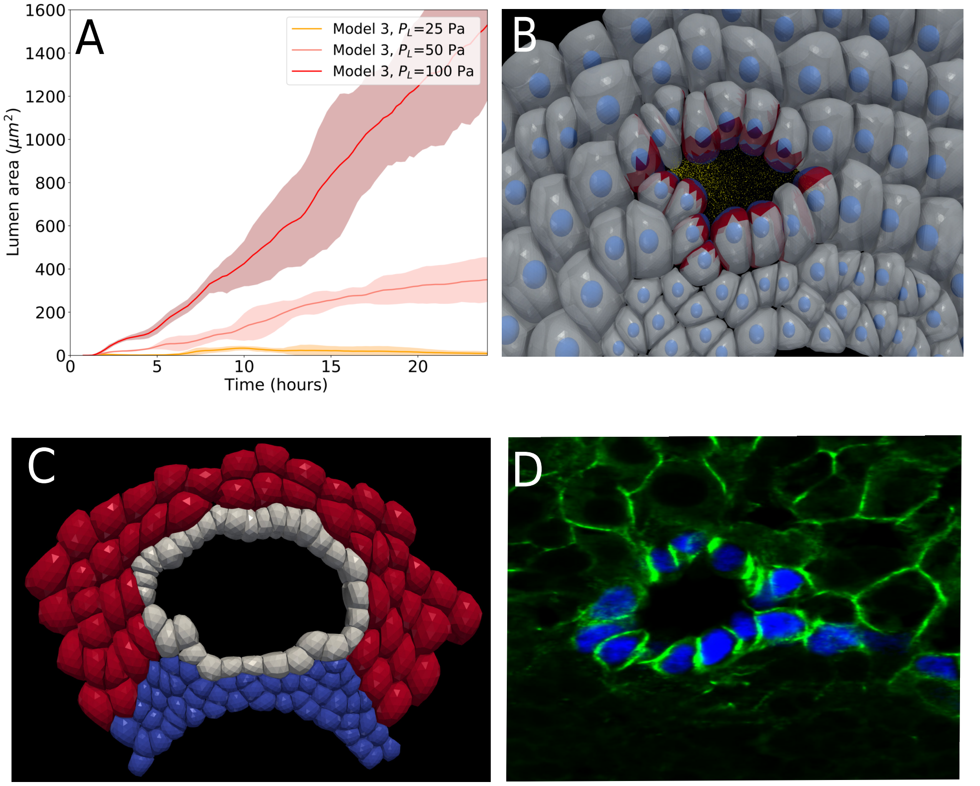

Fig 8. Simulation results for Model 3. A: lumen area versus time for different osmotic pressures. B-C: Snapshot of a simulation for Model 3 ($P_L = 50Pa$ and $P_L = 100Pa$ respectively). In B,the red zones indicate increased cell-cell adhesion due to presence of TJ. D: Picture of typical bile duct lumen for an embryo at E18.5 (SOX9, blue; beta-catenin, green).

Model 3: Model 3 adopts all the characteristics of model 2 and extends the capacity of the cholangiocytes to excrete molecules into the extracellular space inducing an osmotic activity (Fig 8). Expression of ion and water transporters was measured to study possible evidence in favor of the hypothesis that osmotic pressure could be generated at this stage. However, as we have no exact information about the osmotic pressure nor the osmotic activity over time, we simulate different scenarios with varying pressure, assuming that this pressure remains approximately constant over the considered time period. As shown in Fig 8A,C, this hypothesis has a significant impact on the results. For a osmotic pressure $P_L = 25Pa$, lower than the tissue background pressure $P_b = 50Pa$, the lumen size does not become significantly larger than the lumina obtained with Model 1 and Model 2, while similar as in those cases it tends to collapse at the end of the period. However assuming $P_L = 50Pa$ a drastic increase in lumen size can be observed. Interestingly, the lumen size becomes almost stable for $P_L = 50Pa$ while it continues to increase sharply for $P_L = 100Pa$. This shows that a control of osmosis would be an important factor in the lumen stability. In this regard it is also interesting to see how much of the lumen formation can be attributed to apical constriction. To study this question, simulations of Model 3 ($P_L = 50Pa$) have been performed for which AC is restrained. The results, shown in Fig 9B, indicate that the presence of AC (as compared to no AC) speeds up the lumen formation, although it does not seem to play a major role to finally establish a stable lumen. An animation of the simulation can be viewed in SI : Video 6. In conclusion, oriented cell division in combination of osmotic control is able to generate a stable lumen.

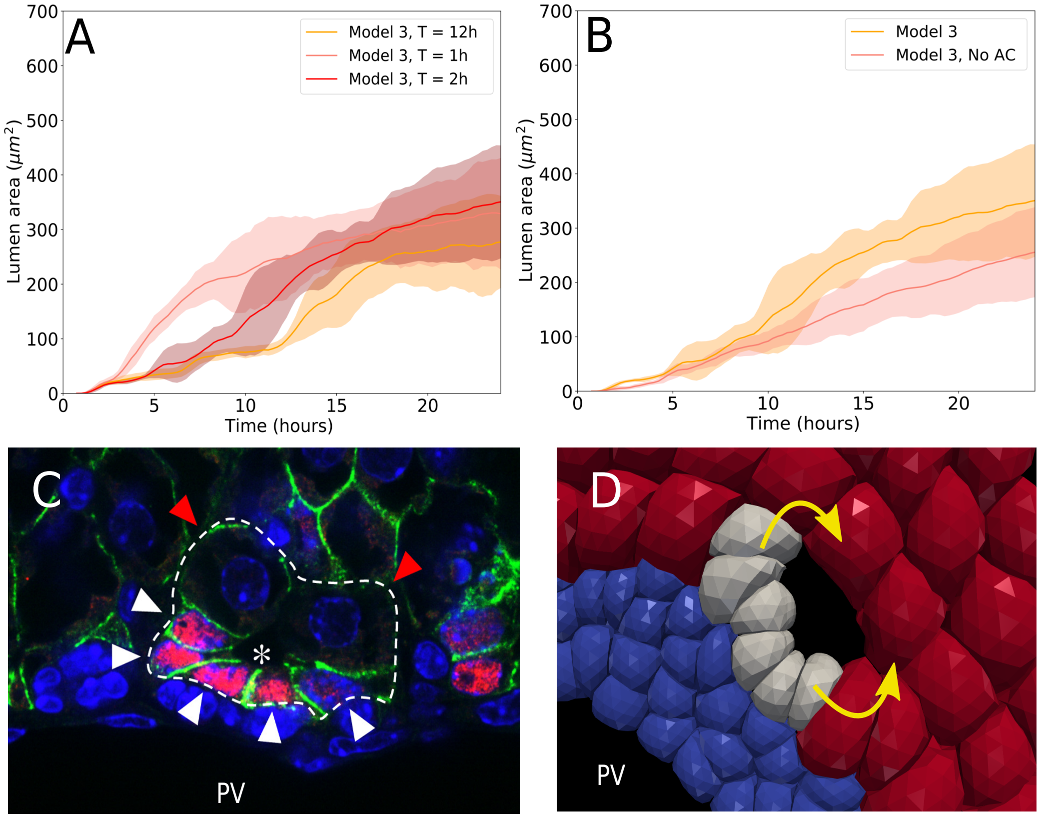

Fig 9. Simulation results for Model 3, assuming $P_l = 50Pa$: lumen area versus time. A: influence of cell-to-cell signalling times T_{sig}. B: influence of absence or presence of Apical constriction (AC). C: Microscopic picture of small lumen with cholangiocytes (white arrowheads) and hepatoblasts (red arrowheads). Tissue section is stained to detect SOX9 (red), beta-catenin (green) and nuclei (DAPI, blue). D: snapshot of simulation showing in comparable configuration. The yellow arrows indicate the direction of cell-cell signalling during the formation.

In a final step, the influence of the cell-to-cell signalling time, i.e the average time it takes for a cholangiocyte to transform a neighboring hepatoblast (Fig 9C,D), on lumen formation has been studied in Model 3. To understand the simulation result, we recall that only hepatoblasts bordering on an initial (possibly initially very small) lumen can differentiate. The signalling time T_{sig} was varied between $1h$ and $12h$. Here, the model runs show (Fig 9A) that the influence is limited to the initial stage of lumen formation, where a short ($T_{sig} = 1$h) favors a quicker onset of lumen formation as compared to the case $T_{sig} = 12h$. This can be mainly attributed the earlier cell division of the cells bordering on the lumen, cfr. point ii) in section Configuration of the in-silico embryonic liver system. Hence, the cell-to-cell signaling time seems to determine the onset of cell division and thereby the time at which the lumen becomes visible. For larger simulation times the difference between the model runs becomes much smaller, as at this point all the cells bordering the lumen have become cholangiocytes and there is no further differentiation.

Discussion and Conclusions

In this paper a model was established to better understand which mechanisms are capable of forming a lumen during bile duct development, using a combined data based and computational model-based strategy. The selection of hypotheses in the computational model was informed by investigations at the molecular level guiding towards several mechanisms controlling lumen formation namely, apico-basal polarization, apical constriction, cell-cell repulsion, creation of apical surfaces, secretion of ions or vesicle exocytosis [9]. In a first step, morphometric data for the building of the computational model of biliary lumenogenesis were collected with a focus on quantifying cell proliferation and apical constriction. Expression of ion and water transporters was measured to identify possible evidence for the hypothesis that osmotic pressure could be generated at the earliest stage of biliary lumenogenesis. Further, bile duct lumen formation occurs as a variant of cord hollowing. Standard cord hollowing is characterized by the creation of a lumen within a cylindrical cord of cells [8]. In bile ducts, the lumen forms between cells that have distinct phenotypes, namely between cholangiocytes and hepatoblasts [4]. Since hepatoblasts differentiate to cholangiocytes during biliary lumenogenesis, the dynamic phenotypic changes of cells lining the developing lumen was equally considered.

In the second step the computational model approach was established to unravel and quantify mechanisms that support lumengenesis. This consists in a cell-centered approach, in which every cell is represented in high detail, permitting to take into account the physical forces that determine the cell shape and motion. The forces that play an essential role in lumen formation embryonic development allegedly are those who originate from (1) pure cell division, (2) apical constriction, or (3) osmotic effects. The goal was to quantify to which level they can influence the lumen formation. To verify those individual force effects, we have at a first stage build an isolated, minimal system of adhering cells free floating in a liquid medium. Our simulations in such an idealized system have shown that each of the three above mentioned effects can indeed induce a lumen formation, provided that the cells are polarized and each of these effects are guided by a polarization vector providing a direction. However, in a real embryonic tissue cells feel continuously "background forces" from the other growing cells. To take this forces into account an in-silico model mimicking the architecture around the portal vein has been built, in which the cell types: mesenchyme, cholangiocytes and hepatoblasts have been distinguished. The underlying assumption was that the local bile duct originates from a single hepatoblast that differentiates to a cholangiocyte, thereby acquiring the capacity to signal to neighboring hepatoblasts. Hereby, our model parameters were informed by the experimentally observed proliferation rates to the hepatoblasts and cholangiocytes. Similar to the minimal system, three submodels have been proposed that rule out the individual effects of the three hypotheses. From the sampling of simulation runs over a period of 24 hours the conclusions were: (i) directed cell division alone can initiate a cavity but cannot maintain this over 24h. (ii) Including apical constriction in the cholangiocytes improves this initial formation but seems not to warrant a stable lumen growth either. In both cases the background pressure forces are to high and induce a collapse of the cavity. (iii) Directed cell division combined with apical constriction and induced osmotic effects of the cholangiocytes creates stable lumen provided that the osmotic pressure is approximately the same as the background pressure of tissue. A too low osmotic effect results eventually in a collapse of the cavity whereas a too high one results in a unlimited growth. We hypothetise that the cholangiocytes adapt the excretion of osmotic molecules to mechanical cues. (iv) The cell-to-cell signalling period controlling the time needed of a cholangiocyte to induce differentiation of an adherent hepatoblast may play are role in the rate of lumen formation, but does not affect its final size.

These findings suggest that bile canaliculi formation may be controlled by mechanisms following the same guiding principle, in particular osmosis. Hence in a last step our established cell-model was used to test this hypothesis in silico.

Supporting information

S1 Text. Supplementary information. This text contains more information about the model algorithms and parameters.

S2 Video 1 Animation of simulation. Cell division provoking cavity formation: Hypothesis I, case polar directed division.

S2 Video 2 Animation of simulation. Cell division provoking cavity formation: Hypothesis I, random directed division.

S2 Video 3 Animation of simulation. Apical constriction provoking cavity formation: Hypothesis II.

S2 Video 4 Animation of simulation. Osmotic effects provoking cavity formation: Hypothesis III.

S2 Video 5 Animation of simulation. Close-up of whole system simulation with bile duct formation (Model 3).

S2 Video 6 Animation of simulation. Whole system simulation with bile duct formation (Model 3).

Acknowledgments

We would like to thank Adrian Ranga for the useful discussion about liver tissue elasticity, and Nicolas Dauguet for help with cell sorting. The work of F.P.L. was supported by D.G. Higher Education and Scientific Research of the French Community of Belgium (grant ARC 15/20-065), the Assistance Publique-Hôpitaux de Paris (France, grant iLITE), the Fonds de la Recherche Scientifique FRS-FNRS (Belgium; grants T.0158.20 and J.0115.20). L.G. holds a PhD fellowship from the Fonds pour la Formation à la Recherche dans l'Industrie et dans l'Agronomie (Belgium: grant 1.E071.18). The work of PvL and DD were supported by the Assistance

Publique-Hôpitaux de Paris (France, grant iLITE) and grant LiSyM by BMBF (German Federal Ministry of Education and Research).

Author contributions

Conceptualization: PVL, LG, FPL, DD; Formal analysis: PVL, LG, AL; Investigation: PVL, LG; Methodology: PVL, LG; Funding acquisition: FPL, DD; Supervision: FPL, DD; Writing: draft PVL, LG; Writing-review editing: PVL, FPL, DD.

SI 1: Model description

Basic DCM forces

In this section the force contributions acting on a cell within the deformable cell model (DCM) are summarized.

Elastic forces cortex

The cell surface in the DCM is triangulated with visco-elastic elements along the edges linking neighbouring nodes. The forces between the nodes mimic the cortical tensions. The membrane envelope is assumed to not significantly contribute to these forces as the presence of caveolae can significantly reduce its mechanical resistance [18]. We assume that cell deformation dynamics can be reasonably approximated by Kelvin-Voigt elements. Consider therefore the internal force F_{int} originating from a Kelvin-Voigt viscoelastic element between node nodes i and j:

$$\begin{aligned}\mathbf{F}_{int,ij} &= \mathbf{F}_{e,ij} - \gamma \mathbf{v}_{ij} \\ &= -k_s(l_{ij} - l_{ij}^0)\mathbf{e}_{ij} - \gamma \mathbf{v}_{ij},\end{aligned} \tag{3}$$

where γ denotes the friction coefficient, $l_{ij}^0 = ||\mathbf{r}_{ij}^0|| = ||\mathbf{r}_j^0 - \mathbf{r}_i^0||$ and $l_{ij} = ||\mathbf{r}_{ij}||$ are the initial (cell at rest) and actual lengths between the nodes, and $\mathbf{v}_{ij} = \mathbf{v}_j - \mathbf{v}_i$ is the relative velocity of nodes i, j. The force balance equation with external forces $\mathbf{F}_{ext}$ demands that $\mathbf{F}_{ext} + \mathbf{F}_{int} = \mathbf{0}$, hence:

$$\mathbf{F}_{ext,ij} - k_s(l_{ij} - l_{ij}^0)\mathbf{e}_{ij} - \gamma \mathbf{v}_{ij} = \mathbf{0}. \tag{4}$$

The linear spring constant for a sixfold symmetric triangulated lattice can be related approximately to the cortex Young modulus E_{cor} with thickness h_{cor} by [65]

$$k_{cor} \approx \frac{2}{\sqrt{3}} E_{cor} h_{cor}. \tag{5}$$

Besides tension, the cortex resists to bending. The bending resistance in the cortex is incorporated by the angular resistance of the hinges determined by two adjacent triangles $T_1 = \{ijk\}$ and $T_2 = \{ijl\}$. This can be accounted for by the bending moment M:

$$M = k_b sin(\theta - \theta_0) \tag{6}$$

where k_b is the bending constant, and θ is is the angle between the normal vectors to the triangles $\mathbf{n}_\alpha, \mathbf{n}_\beta$ by their scalar product $(\mathbf{n}_\alpha \mathbf{n}_\beta) = cos(\theta)$. θ_0 is the angle of spontaneous curvature. A spontaneous curvature denotes the curvature for which the bending energy is zero.

The moment M can be transformed to an equivalent force system $\mathbf{F}_{m,z}$ $(z \in \{ijl\})$ for the triangles T_1 and T_2 where here for T_1 we can compute $\mathbf{F}_{m,i} = M/l_1 \mathbf{n}_1$ using l_1

as the distance between the hinge of the triangle pair and the point i, and similar expression for $\mathbf{F}_{m,l}$. The forces working on nodes j, k must at least fulfill $\mathbf{F}_{m,i} + \mathbf{F}_{m,j} + \mathbf{F}_{m,k} + \mathbf{F}_{m,l} = 0$ to conserve total momentum, see e.g. [32, 64]. The bending stiffness of the cortex is approximated by

$$k_b \approx \frac{E_{cor} h^3}{12(1-\nu^2)}, \tag{7}$$

where $\nu \approx 0.5$ is the Poisson's ratio of the cortex. Note that the elastic modulus of the cortex, E_{cor} enters both, the bending force and the tension force.

Volume forces

The volume change of the cell depends on the applied pressure and the cell bulk modulus K_V. The total compressibility of the cell depends on volume fraction of water in the cytosol, the cytoskeleton (CSK) volume fraction and structure, and the compressibility of the individual organelles. In addition, it may be influenced by the permeability of the plasma membrane for water, the presence of caveolae, and active responses inside and of the cell. We calculate the internal pressure in a cell by the logarithmic strain for volume change:

$$p = -K_V log(\frac{V}{V_0}), \tag{8}$$

whereby V is the actual volume and V_0 is the reference volume i.e., the volume of the cell not subject to compression forces. For small deviations of V from V_0, $p \approx K_V (V - V_0)/V_0$. Within our model the volume V of the cell is computed summing up the volumes of the individual tetrahedra that build up the cell. The nodal force is obtained by multiplying the pressure with the nodal Voronoi area S_i (see [63]), i.e. $\mathbf{F}_{vol,i} = pS_i\mathbf{R}_i$ where the local curvature vector $\mathbf{R}_i$ is computed for that node using a discrete Laplace-Beltrami operator [25].

Contact model and adhesive forces

Whereas in a CBM, cells interact through central forces described by (modified) Hertz or JKR theory for adhesive spheres, in DCM the interaction forces need to be defined for each node individually, thereby endowing a representation of local surface heterogeneities. The approach followed in this work adopts a discretised Maugis-Dugdale theory. The Maugis-Dugdale theory for adhering bodies is a generalization of the JKR theory for spheres [60]. This theory captures the full range between the Derjaguin-Muller-Toporov (DMT) zone of long reaching adhesive forces of a soft homogeneous isotropic elastic sphere and small adhesive deformations in the Johnson-Kendall-Roberts (JKR)-limit of a hard homogeneous isotropic elastic sphere of short interaction ranges. Here, we assign to each triangle of the cell surface a circumscribing sphere reflecting the local curvature. Two triangles belonging to different cells can locally interact by collision of their assigned spheres. To compute the magnitude of these interactions, we use the general Maugis-Dugdale stress formula, which are integrated over the common contact area between the triangles, see [25, 64] for more details. The adhesion force is fully determined by the specific adhesion energy W and the typical effective adhesive range h_0 that reflects the attractive cutoff distance between the bodies. We set $h_0 = 2 \cdot 10^{-8} m$ in all the simulations [61].

In our model, Maugis-Dugdale theory is applied to every set of triangles which constitute the cell surface. A varying number of cadherin bonds is mimicked by varying the adhesion energy along the cell surface triangles.

Migration forces

In models in which cell movement and deformation is mimicked by force-balance equations following Newton's law of motion as this is the case for the DCM and CBM, migration is usually modelled by an active migration force $\mathbf{F}^{mig}$ representing the random micro-motility of a cell. For the sake of simplicity the cell shape, filopodia etc. movements during migration are not detailed in the model but instead the different mechanisms in cell migration is lumped into one net force which is uniformly distributed to the nodes the cell if not mentioned otherwise. For specific applications, the forces might be non-uniformly distributed. In absence of influences that impose a certain direction or persistence, it is commonly assumed that the migration force is stochastic, formally resulting in $\mathbf{F}^{mig} = \mathbf{F}^{ran}$, with $\langle \mathbf{F}^{ran} \rangle = \mathbf{0}$, and $\langle \mathbf{F}^{ran}(t) \otimes \mathbf{F}^{ran}(t') \rangle = \mathbf{M}\delta(t - t')$, where $\mathbf{M}$ is an amplitude 3×3 matrix and relates to the diffusion tensor $\mathbf{D}$ of the cell. As cell migration is active, depending on the local matrix density and orientation of matrix fibers, the autocorrelation amplitude matrix $\mathbf{M}$ cannot a priori be assumed to follow a fluctuation-dissipation (FD) theorem. However, "measuring" the position of a cell in the simulations the position autocorrelation function might be experimentally used to determine the diffusion tensor using $\langle ((\mathbf{r}(t + \tau) - \mathbf{r}(t)) \otimes (\mathbf{r}(t + \tau) - \mathbf{r}(t)) \rangle = 6\mathbf{D}\tau$, and $\mathbf{M}$ be calibrated such that the numerical solution of the equation of motion for the cell position reproduces the experimental result for the position-autocorrelation function. For example, in a homogeneous environment $\mathbf{M}$ can be casted into a form formally equivalent to the FD-theorem, leading to an k_BT-equivalent for cellular systems, that is controlled by the cell itself [43, 44].

Note, we assume here a momentum transfer to the ECM by applying the ECM friction and active micro-motility term, but we do not model the ECM explicitly.

Cell cycle and cell division

During cytokinesis, the continuous shrinking of the contractile ring, together with the separation of the mitotic spindle, gradually divides the mother cell into two daughter cells. After mitosis the cell has split up in two adhering cells. Such a process of cell division in 2D deformable cells has been previously described (e.g. [24]) but it can be costly and tedious to perform in 3D.

As we are merely interested in long term effects (i.e. hundreds of cell divisions), and as the cytokinesis is a short process compared to the duration of the entire cell cycle, we avoid these particular tedious intermediate steps in our model, and directly create two new adhering cells that are within the shape of the mother cells just before its division using the algorithm established in ref. [34]. In the model, cells grow by increasing their volume and surface and they can divide when their actual volume reaches the double of the initial value. The orientation of cell division can be chosen randomly (as is the case for non polarized hepatocytes) or with a preferred direction. The latter is the case when a polarized cell divides. In this case the division direction is the polarization vector. As observed experimentally, we also implement a temporary and short rounding up period just before cells division. This has a consequence that the cell volume slightly drops and hence the pressure inside the cell increases, causing a rounding of the surface. The shortening of the vertex edges is chosen such that this pressure increase is not more than 100 to 200 Pa, achieved by modifying the lengths from l_0 to $0.95 * l_0$. The rounding up period in our model does not take more than 5% of the total cell cycle time.

The cells in our system can either be proliferating or quiescent. Immediately after cell division, all cells are assumed to proliferate. A change to quiescence is here assumed to be induced by chemical signals of other cells. To ensure in the simulations that only the fraction of the cells is growing conform with the experimental observations, an algorithm is invoked that sweeps every time step over a certain cell type and ensures that the prescribed fraction of proliferating cells is maintained. The picking of cells that need to go to quiescence is done in a random way. This algorithm was chosen as the mechanistic control of how many cells divide was not subject of the present simulation study.

DCM extension: Polarity vector

A normalized polarity vector $\vec{P}$ (PCP) is assigned to each of the cells. This vector defines for every cell two opposite conical polar regions (see Fig 2A). The triangular regions on the cell surface that are marked as polar are defined by the scalar product condition:

$$\|\vec{P} \cdot \vec{N}_i\| < a, \tag{9}$$

where N_i is a normalized vector with origin the center of mass of the cell, and pointing to a triangle i. To define the area of the polar region a can be chosen according to $0 < a < 1$. We chose in the simulations of this work $a = 0.7$. This corresponds to a bi-conical area with angle α of approximately 60 degrees. The polar regions (triangles) may have different physical properties than the rest of the cell surface, such as a different specific adhesion energy. The PCP vector is assumed to be perpendicular to the apical vector, which is enforced in the model with every timestep.

DCM extensions : apical vector, apical constriction and tight junctions

Every cell also has an apical vector $\vec{A}$ (ABP), which defines the apical and basal side of the cell. Similar to the polar regions, the apical and basal triangular regions on the cell surface are defined by the conditions:

$$\vec{A} \cdot \vec{N}_i > b \text{ (apical region)} \tag{10}$$

and

$$\vec{A} \cdot \vec{N}_i < -b \text{ (basal region)} \tag{11}$$

Like with the polar vector, this corresponds to a conical area with angle β and the scalar value of $b \in [0, 1]$ determines the area of the regions, however the difference is that the apical side of the cell may have different physical properties than the basal side. In this work the cortical cytoskeleton on the apical side can contract, causing apical constriction.

In the model, the apical vector is forced to point towards the principal region where the cell surface has the least contact area with other cells in line with the assumption made, that the apical forms the cell's interface with the lumen. $\vec{A}$ is obtained by

$$\vec{A} = \sum_i \vec{N}_i / \| \sum_i \vec{N}_i \|. \tag{12}$$

$\vec{N_i}$ of the triangle now must not be in contact with another triangle from another cell. These conditions can for example be fulfilled when gaps between cells are created due to osmotic effects (e.g. onset of a small cavity). $\vec{A}$ is updated every timestep, except during cell division and a short relaxation phase right after cell division.

Adherent cells can also develop tight junctions (TJ) between them. In the model, we define for every cell that has an apical vector, a region with TJ triangles i that fulfill the condition :

$$\vec{A} \cdot \vec{N}_i > c_1 \text{ and } \vec{A} \cdot \vec{N}_i < c_2 \tag{13}$$

Here c_1 and c_2 are the limit values that define a conical ribbon along the cell where TJ can be present (see Fig 2D). The parameter values for c_1 and c_2 are chosen such that the ribbon is about 1 or maximum 2 triangles thick. As TJ are areas on the cell surface with a reinforced connection, a larger specific adhesion energy is assigned to these areas than to the other surface areas. As such, when two triangles of different cells with a TJ come into contact, the force necessary to separate them will be much higher than for normal cell-cell contacts.

The apical constriction on the apical side is modeled as a shortening of the equilibrium element lengths between connected nodes that are located within the apical region (see below). This results in a movement of the two nodes towards each other. The shortening operation is executed only once. After a certain relaxation time a new global force equilibrium is reached between the nodes. The modification of the equilibrium element lengths of the nodal springs during apical constriction are computed assuming two different zones:

$$l_0 := l_0 * d_2 \text{ for: } \vec{A} \cdot \vec{N}_i > c_2 \text{ and } \vec{A} \cdot \vec{N}_i < c_1, \tag{14}$$

which is the zone of the tight junctions, and

$$l_0 := l_0 * d_1 \text{ for: } \vec{A} \cdot \vec{N}_i > c_1. \tag{15}$$

in the apical domain.

To simulate the presence of an apical circumferential ring, the strongest constriction is applied in the zone of the TJ ribbon, whereas a lower constriction is applied in the apical domain ($0 < d_2 < d_1 < 1$). We have adopted the values $d_2 = 0.5$ and $d_1 = 0.7$. This warrants a strong contraction. Moreover, the adhesive energy on the apical side is assumed to be lower than elsewhere on the cell because generally one observes that cadherin staining is less strong there (see Fig 10B).

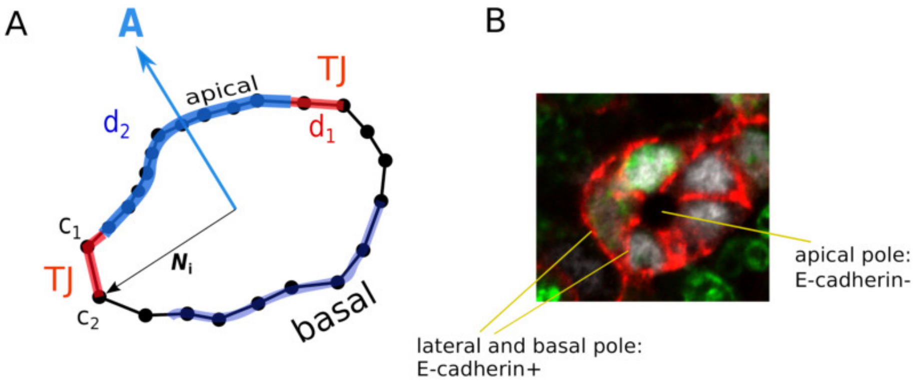

Fig 10. Cartoon indicating the parameters needed to determine the apical domain and apical circumferential ring.

DCM extensions : Osmotic effects and signalling

We assume that osmotic forces in the system result from differences of solutes e.g by molecules such as salts that are released from the cell into the extracellular space. These molecules further diffuse locally and cause a concentration gradient with more distant locations. For example, if one cell starts to excrete ions, a salt concentration gradient is generated attracting water molecules towards the cell potentially causing a hydrostatic pressure increase strong enough to push away cells in the direct neighborhood of the central cell. As a consequence an extracellular space can arise, depending in shape and size on the dynamics and mechanics of the surrounding cells. One way to simulate the diffusion process of salts and flow of water could be to solve a system of partial differential equations (PDEs) for diffusive transport of salt and the advection of water. As the surrounding cells reorganise during the lumen formation process and hence the shape of the extracellular space changes, the boundary conditions for the PDEs change constantly. The constant change requires high resolution meshing and constant re-meshing of the complex cavity, which is numerically complicated and computationally time consuming. To alleviate this, inspired by smoothed particle hydrodynamics methods [62], we introduce the concept of “tracer particles (TP)”, which are small ”inert” particles. They can diffuse freely inside the cell or in the extracellular space without mutual interaction (see Fig 2D). All the tracer particles (about 1000 in numbers) are initially inside the cell and start diffusing from there. The advantage of using particles to mimic the fluid is that their motion can be simulated by a Newton’s equation of motion as for the cells, hence the coupling of fluid movement and cell deformation is straightforward.

The force on each particle originates principally from Brownian motion as and its magnitude is controlled by the TP diffusion coefficient. Additionally, a small force component is exerted to them in the apical direction to facilitate their movement towards the apical side which can be justified by directional vesicle transport towards lumen in polarized cells [7].

To ensure that the particles can move outside the cell only in a certain region, we define a “transparent” region for each cell surface through which these particles can move into the extracellular space. The transparent region is equal to the apical side of the cells. In other parts of the cell, the particles cannot move across the cell surface. The particles can thus locally cross the cell boundary when moving from inside to outside, but are always repelled when trying to move back from the outside to the inside of the cell. We note that these particles do not represent individual ions but rather the local density of ions. Nevertheless, to ensure the diffusive speed is similar to the ions, the particles are assigned with the diffusion coefficient of the ion species.

In the extracellular space a tracer particles marks a triangle if it is in close proximity of that triangle representing a free cell surface piece, not in full contact with another cell. As there are many TP present, all free surface areas of a cell will progressively become marked. To simulate the resulting hydrostatic pressure on that cell, each marked triangle receives an external force $\vec{F}_{osm} = PA_i\vec{n}_i$, where P is the assumed hydrostatic pressure that corresponds to the osmotic pressure generated by the difference in ion concentration (assumed constant here), and A_i is the surface of the marked triangle. Triangles belonging to two different cells that are in contact will only have a negligible probability to be marked as the particles cannot access the space between them.

Basic CBM forces

The CBM does not resolve cell shape. Forces are in the CBM are assumed to be exerted on the center of mass of the cell.

CBM: Adhesive and repulsive forces

In the CBM, cells are approximated by homogeneous, isotropic, elastic and adhesive spheres which split into two adherent cells during mitosis. Under conditions met in this work [12, 41], the total cell to cell interaction force can be approximated by the sum of a repulsive and an adhesive force :

$$\vec{F}_{cc} = \vec{F}_{rep} + \vec{F}_{adh}. \tag{16}$$

The repulsive part is a modified Hertz contact force (see main text) taking into account the effects of multiple cell to cell contacts.

The adhesive force term between cells can be estimated as proportional to the contact area and the energy of the adhesive contact W [43]:

$$F_{adh,ij} = -\pi W R_{ij}. \tag{17}$$

CBM: Migration forces

The same principles for modeling the migration force in the DCM are applied to the CBM, whereby the migration force in the CBM is directly applied to the cell center.

CBM: Cell division

As in the DCM, if the cell passed a critical volume $V_{crit} = 2V_{0,i}$, the cell undergoes mitosis and two new cells with volume $V_{0,i}/2$ are created. A simplified version of the division algorithm consists of placing directly two smaller daughter cells in the space originally filled by the mother cell at the end of the interphase [13, 41]. When the two daughter cells are created, their reorganize in space driven by their cell-cell interaction force as well as the interaction forces of the two daughter cells with their other surrounding cells until mechanical equilibrium is reached. If the space filled by the mother cell is small, which is often the case for cells in the interior of a cell population, the local interaction forces occurring after replacing the mother cell by two spherical daughters, can adopt large (un-physiological) values leading to unrealistic large cell displacements. This might be circumvented by intermediately reducing the forces between the daughter cells (see below) [41]. Alternatively, cells could in small steps be deformed during cytokinesis into dumbbells before splitting [38]. In this work we pursue the simpler approach as it resembles the cell division algorithm we use for the DCM.

Cell-to-cell signalling

In our model, we assume that Notch-jagged signaling between cholangiocytes and hepatocytes is governed by several of conditions. First, we assume that their common contact area must be sufficiently high. Thus, a minimal number of triangles (or surface area) of both cells must be in mutual contact: $A_T > A_{min}$, where A_T is the total contact area between two cells, and the parameter A_{min} is set arbitrarily to 20% of the cell surface. We found that this parameter does not influence the results significantly provided that A_{min} is larger than zero. However, this condition alone is not enough for a hepatocyte to transform in a cholangiocytes, as then any hepatocyte in the tissue adjacent to a cholangiocytes would be able to transform at some point, causing a homogeneous spread of cholangiocytes which is not observed experimentally. Hence, the second condition for the transformation is that the hepatocyte must delimit an existing (possibly small) lumen. Third, we also need to introduce a transition contact time T_{sig} which specifies the minimum time the signalling needs in order for a hepatocyte to change to a cholangiocyte. A value $T_{sig} = 0$ would mean here that the transformation is immediate, which is not observed as some hepatocytes may express weak SOX9+ signals but have a much larger size than a mature cholangiocyte. The signaling time is likely limited by the cell cycle time. When a hepatocyte gets the signal to transform, we assume that it will be fully differentiated upon the next cell division. We set here $T_{sig} = 2h$ as default value.

Initialization of model and boundary conditions of bile-duct system

The cells are initially positioned side by side on concentric circles with curvature determined by the radius of the portal vein. The most inner layer represents the portal vein endothelial for which we assume the positions are fixed during the simulations. The second layer are the mesenchyme, followed by the hepatoblasts, partially represented by the DCM and the outer layers fully represented by the CBM.

A background pressure P_b of the CBM hepatoblasts needs to be exerted at the outer border of the segment as a result of radial tissue growth and resistance from nearby cells. This is achieved in the model by exerting an inward body force to the outermost border cells such that the inner hepatoblasts represented by the DCM have an average internal pressure of P_b. For the DCM, the pressure is calculated by Eq.8. For the CBM the pressure p_i on a cell i is derived from the viral stress and given by:

$$p_i = \frac{1}{3} tr(\sigma_i) \text{ , with } \sigma_i = \frac{1}{\mathcal{V}_i} \sum_j \left(\vec{F}_{ij} \otimes \vec{r}_{ij} \right) \tag{18}$$

being the stress tensor quantifying the stresses cell i experiences subject to contact forces $\vec{F}_{ij}$ with other cells j [43]. Here, $\vec{r}_{ij}$ is the vector pointing from the center of cell i to the cell j with $||\vec{r}_{ij}|| = d_{ij}/2$ and $\mathcal{V}_i$ is the *sampling* volume which can be taken as the cell volume.

To ensure the cells remain in a planar configuration, we apply a small penalty force on the center-of-mass of all the cells each time the center of mass moves away from the XY plane. A simulation then starts in which only the cells positions are updated and a mechanical equilibrium is reached. This configuration is then used for all further simulations.

Calculation of the bile duct lumen area

We obtain the lumen area by considering the triangles of the cells that are marked by tracer particles. The procedure to compute the lumen volume is conceptually similar to how the volume of a cell given its triangulated structure is computed (see ref. [34]). First, the geometric center of all these triangles is computed, resulting in a vector pointing to the geometric center of the bile duct. From this point, we compute the signed volume of a tetrahedron with as base a marked triangle and top the center. This is done for all marked triangles, and subsequently these volumes are then summed up. This gives a reasonable estimation of the volume confined by the marked cells.

Computational scheme executed during simulation

In Fig 11 , a model flow chart is given with the principal algorithms that are executed every timestep. The algorithms that are cell -type dependent, are colored according to the cell type.

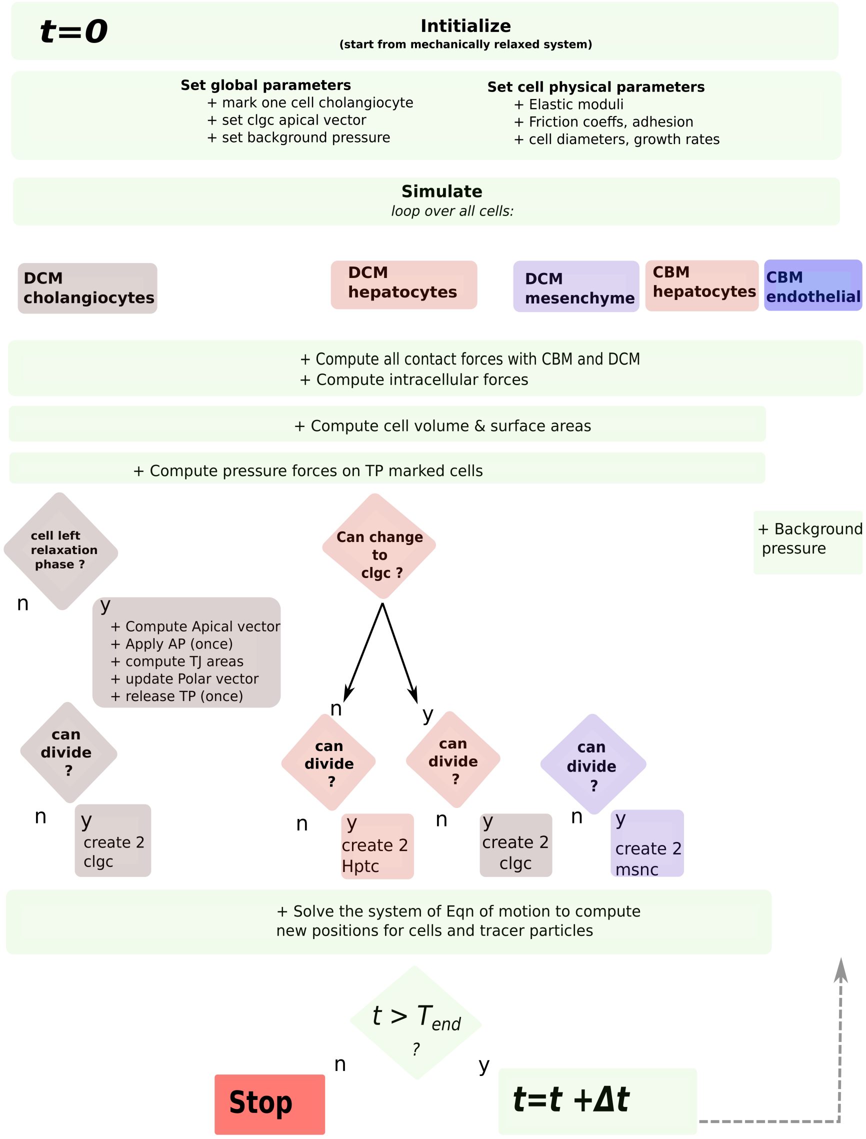

Fig 11. Computational scheme executed during simulation.

References

1. Gordillo M, Evans T, Gouon-Evans V. Orchestrating liver development Development 2015 142: 2094-2108; doi: 10.1242/dev.114215
2. Ober EA, Lemaigre FP. Development of the liver: Insights into organ and tissue morphogenesis; Journal of Hepatology. 2018; doi:10.1016/j.jhep.2018.01.005
3. Lemaigre FP. Development of the Intrahepatic and Extrahepatic Biliary Tract: A Framework for Understanding Congenital Diseases. Annual Review of Pathology: Mechanisms of Disease. 2020;doi:10.1146/annurev-pathmechdis-012418-013013.
4. Antoniou A, Raynaud P, Cordi S, Zong Y, Tronche F, Stanger BZ, et al. Intrahepatic Bile Ducts Develop According to a New Mode of Tubulogenesis Regulated by the Transcription Factor SOX9. Gastroenterology. 2009;doi:10.1053/j.gastro.2009.02.051.
5. Takashima Y, Terada M, Kawabata M, Suzuki A. Dynamic three-dimensional morphogenesis of intrahepatic bile ducts in mouse liver development. Hepatology. 2015;doi:10.1002/hep.27436.
6. Tanimizu N, Kaneko K, Itoh T, Ichinohe N, Ishii M, Mizuguchi T, et al. Intrahepatic bile ducts are developed through formation of homogeneous continuous luminal network and its dynamic rearrangement in mice. Hepatology. 2016;doi:10.1002/hep.28521.
7. Benhamouche-Trouillet S, O'Loughlin E, Liu CH, Polacheck W, Fitamant J, McKee M, et al. Proliferation-independent role of NF2 (Merlin) in limiting biliary morphogenesis. Development (Cambridge). 2018;doi:10.1242/dev.162123.
8. Lubarsky B, Krasnow MA. Tube morphogenesis: Making and shaping biological tubes Cell 2003 Jan 10;112(1):19-28. doi: 10.1016/s0092-8674(02)01283-7.
9. Datta A, Bryant DM, Mostov KE. Molecular regulation of lumen morphogenesis; Curr Biol 2011 Feb 8;21(3):R126-36. doi: 10.1016/j.cub.2010.12.003.
10. Blasky AJ, Mangan A, Prekeris R. Polarized Protein Transport and Lumen Formation During Epithelial Tissue Morphogenesis. Annual Review of Cell and Developmental Biology. 2015;doi:10.1146/annurev-cellbio-100814-125323.
11. Zong Y, Panikkar A, Xu J, Antoniou A, Raynaud P, Lemaigre F, et al. Notch signaling controls liver development by regulating biliary differentiation. Development. 2009;doi:10.1242/dev.029140.
12. Drasdo D, Hoehme S, Block M. On the Role of Physics in the Growth and Pattern Formation of Multi-Cellular Systems: What can we Learn from Individual-Cell Based Models. Journal of Statistical Physics. 2007;128:287–345.
13. Schaller G, Meyer-Hermann M. Multicellular tumor spheroid in an off-lattice Voronoi-Delaunay cell model. Phys Rev E. 2005;71(5):51910. doi:10.1103/PhysRevE.71.051910.
14. Geris L, Van Liedekerke P, Smeets B, Tijskens E, Ramon H. A cell based modelling framework for skeletal tissue engineering applications Journal of biomechanics. 2010; 43(7)

15. Vermolen, F J, Gefen A. A semi-stochastic cell-based formalism to model the dynamics of migration of cells in colonies Biomechanics and Modeling in Mechanobiology. 2012;11(1). doi:10.1007/s10237-011-0302-6

16. Schlueter D.K., Ramis-Conde I, Chaplain M.A.J. Multi-scale modelling of the dynamics of cell colonies: insights into cell adhesion forces and cancer invasion from in silico simulations J. R. Soc. Interface 12: 20141080. doi:10.1098/rsif.2014.1080

17. Basan M, Prost J, Joanny JF, Elgeti J. Dissipative particle dynamics simulations for biological tissues: rheology and competition. Physical biology. 2011;8(2):26014. doi:10.1088/1478-3975/8/2/026014.

18. Van Liedekerke P, Neitsch J, Johann T, Alessandri K, Nassoy P, Drasdo D. Quantitative agent-based modeling reveals mechanical stress response of growing tumor spheroids is predictable over various growth conditions and cell lines. PLoS Computational Biology. 2019;doi:10.1371/journal.pcbi.1006273.

19. A. Ghaffarizadeh, R. Heiland, S.H. Friedman, S.M. Mumenthaler, and P. Macklin, PhysiCell: an open source physics-based cell simulator for 3-D multicellular systems PLoS Comput. Biol. 14(2): e1005991, 2018. DOI: 10.1371/journal.pcbi.1005991.

20. Delile J., Herrmann M., Peyriéras N, Doursat R. A cell-based computational model of early embryogenesis coupling mechanical behaviour and gene regulation. newblock Nat Commun 8, 13929 (2017). https://doi.org/10.1038/ncomms13929

21. González-Valverde, I., García-Aznar, J.M. An agent-based and FE approach to simulate cell jamming and collective motion in epithelial layers. Comp. Part. Mech. 6, 85–96 (2019). https://doi.org/10.1007/s40571-018-0199-2

22. Katarzyna A. Rejniak An immersed boundary framework for modelling the growth of individual cells: An application to the early tumour development Journal of Theoretical Biology.2007 doi.org/10.1016/j.jtbi.2007.02.019

23. Fedosov DA, Caswell B, Karniadakis GE. Systematic coarse-graining of spectrin-level red blood cell models. Computer Methods in Applied Mechanics and Engineering. 2010;199(29–32):1937–1948. doi:10.1016/j.cma.2010.02.001.

24. Jamali Y, Azimi M, Mofrad M RK, A sub-cellular viscoelastic model for cell population mechanics PLoS One. 2010; doi:10.1371/journal.pone.0012097

25. Odenthal T, Smeets B, Van Liedekerke P, Tijskens E, Van Oosterwyck H, Ramon H. Analysis of Initial Cell Spreading Using Mechanistic Contact Formulations for a Deformable Cell Model. PLoS Computational Biology. 2013;9(10):e1003267. doi:10.1371/journal.pcbi.1003267.

26. Tozluoğlu, M., Tournier, A., Jenkins, R. et al. Matrix geometry determines optimal cancer cell migration strategy and modulates response to interventions. Nat Cell Biol, 2013. doi: 10.1038/ncb2775

27. Sandersius SA, Weijer CJ, Newman TJ. Emergent cell and tissue dynamics from subcellular modeling of active biomechanical processes. Physical Biology. 2011;8:45007.

28. Tanaka S, Sichau D, Iber D. LBIBCell: a cell-based simulation environment for morphogenetic problems. Bioinformatics. 2015;doi:10.1093/bioinformatics/btv147.

29. Hirashima T, Rens E.G., Merks R.M.H. Cellular Potts Modeling of Complex Multicellular Behaviors in Tissue Morphogenesis Dev Growth Differ. 2017 DOI: 10.1111/dgd.12358

30. Bessonov N., Volpert V. Deformable Cell Model of Tissue Growth Computation 2017, doi: 10.3390/computation5040045

31. Chen J, Weihs D,Van Dijk, M, Vermolen Fred J. A phenomenological model for cell and nucleus deformation during cancer metastasis, Biomechanics and Modeling in Mechanobiology. 2018. doi:10.1007/s10237-018-1036-5

32. Smeets B, Cuvelier M, Pešek J, Ramon H. The Effect of Cortical Elasticity and Active Tension on Cell Adhesion Mechanics. Biophys J. 2019. doi:10.1016/j.bpj.2019.01.015

33. Ioannou F., Dawi Malik A., Tetley Robert J., Mao Yanlan, Muñoz José J Development of a New 3D Hybrid Model for Epithelia Morphogenesis Frontiers in Bioengineering and Biotechnology 2020, DOI=10.3389/fbioe.2020.00405

34. Van Liedekerke P, Neitsch J, Johann T, Warmt E, Gonzàlez-Valverde I, Hoehme S, et al. A quantitative high-resolution computational mechanics cell model for growing and regenerating tissues. Biomechanics and Modeling in Mechanobiology. 2020;doi:10.1007/s10237-019-01204-7.

35. Gong S, Zheng C, Doughty ML, Losos K, Didkovsky N, Schambra UB, Nowak NJ, et al. A gene expression atlas of the central nervous system based on bacterial artificial chromosomes. Nature 2003, doi: 10.1038/nature02033

36. Nissen SB, Rønhild S, Trusina A, Sneppen K. Theoretical tool bridging cell polarities with development of robust morphologies. eLife. 2018;doi:10.7554/eLife.38407.

37. Martin, A. C., Goldstein, B. . Apical constriction: themes and variations on a cellular mechanism driving morphogenesis. Development, 141(10), 1987-1998. doi: 10.1242/dev.102228

38. Hoehme S, Brulport M, Bauer A, Bedawy E, Schormann W, Hermes M, et al. Prediction and validation of cell alignment along microvessels as order principle to restore tissue architecture in liver regeneration. Proceedings of the National Academy of Sciences. 2010;107(23):10371–10376.

39. Brugues J, Maugis B,Casademunt J,Nassoy P, Amblard F, Sens, P Dynamical organization of the cytoskeletal cortex probed by micropipette aspiration. PNAS. 2010, doi: 10.1073/pnas.0913669107

40. Tinevez JY, Schulze U, Salbreux G, Roensch J, Joanny JF, Paluch E. Role of cortical tension in bleb growth. Proceedings of the National Academy of Sciences of the United States of America. 2009;106(44):18581–6. doi:10.1073/pnas.0903353106.

41. Galle J, Loeffler M, Drasdo D. Modeling the effect of deregulated proliferation and apoptosis on the growth dynamics of epithelial cell populations in vitro. Biophysical journal. 2005;88(1):62–75.

42. Buske P, Galle J, Barker N, Aust G, Clevers H, Loeffler M. A Comprehensive Model of the Spatio-Temporal Stem Cell and Tissue Organisation in the Intestinal Crypt. PLoS Comput Biol. 2011;7(1):e1001045. doi:10.1371/journal.pcbi.1001045.

43. Van Liedekerke P, Palm MM, Jagiella N, Drasdo D. Simulating tissue mechanics with agent-based models: concepts, perspectives and some novel results. Computational Particle Mechanics. 2015;2(4):401–444. doi:10.1007/s40571-015-0082-3.

44. Drasdo D, Hoehme S. Modeling the impact of granular embedding media, and pulling versus pushing cells on growing cell clones. New Journal of Physics. 2012;14(5):55025.

45. Chu YS, Dufour S, Thiery JP, Perez E, Pincet F. Johnson-Kendall-Roberts Theory Applied to Living Cells. Physical Review Letters. 2005;94(2):28102. doi:10.1103/PhysRevLett.94.028102.

46. Wilding Crawford L, Foley JF, Elmore SA. Histology atlas of the developing mouse hepatobiliary system with emphasis on embryonic days 9.5-18.5. Toxicologic Pathology. 2010;doi:10.1177/0192623310374329.

47. Boyer JL. Bile formation and secretion. Comprehensive Physiology. 2013;doi:10.1002/cphy.c120027.

48. Tabibian JH, Masyuk AI, Masyuk TV, O'Hara SP, LaRusso NF. Physiology of cholangiocytes. Comprehensive Physiology. 2013;doi:10.1002/cphy.c120019.

49. Buckling instabilities of one-layered growing tissues. Phys Rev Lett 84:4244–4247 (2000). doi:10.1103/PhysRevLett.84.4244

50. Inoue, Y., Tateo, I. , Adachi, T. Epithelial tissue folding pattern in confined geometry. Biomech Model Mechanobiol 19, 815–822 (2020). doi:10.1007/s10237-019-01249-8.

51. Gloerich M, Bianchini JM, Siemers KA, Cohen DJ, Nelson WJ. Cell division orientation is coupled to cell-cell adhesion by the E-cadherin/LGN complex. Nature Communications. 2017;doi:10.1038/ncomms13996.

52. Overeem AW, Bryant DM, van IJzendoorn SC. Mechanisms of apical-basal axis orientation and epithelial lumen positioning.* Trends Cell Biol. 2015. doi:10.1016/j.tcb.2015.04.002

53. Fletcher AG, Osterfield M, Baker RE, Shvartsman SY. Vertex models of epithelial morphogenesis. Biophys J. 2014. doi:10.1016/j.bpj.2013.11.4498

54. Inoue Y, Suzuki M, Watanabe T, Yasue N, Tateo I, Adachi T, et al. Mechanical roles of apical constriction, cell elongation, and cell migration during neural tube formation in Xenopus. Biomechanics and Modeling in Mechanobiology. 2016;doi:10.1007/s10237-016-0794-1.

55. Okuda S, Takata N, Hasegawa Y, Kawada M, Inoue Y, Adachi T, et al. Strain-triggered mechanical feedback in self-organizing optic-cup morphogenesis. Science Advances. 2018;doi:10.1126/sciadv.aau1354.

56. Citi S. The mechanobiology of tight junctions; 2019. Biophys Rev 11, 783–793 (2019). https://doi.org/10.1007/s12551-019-00582-7

57. Desai SS, Tung JC, Zhou VX, Grenert JP, Malato Y, Rezvani M, et al. Physiological ranges of matrix rigidity modulate primary mouse hepatocyte function in part through hepatocyte nuclear factor 4 alpha. Hepatology. 2016;doi:10.1002/hep.28450.

58. Yang L, Wang WH, Qiu WL, Guo Z, Bi E, Xu CR. A single-cell transcriptomic analysis reveals precise pathways and regulatory mechanisms underlying hepatoblast differentiation. Hepatology. 2017;doi:10.1002/hep.29353.

59. Tanimizu N, Kikkawa Y, Mitaka T, Miyajima A. 1- and 5-containing laminins regulate the development of bile ducts via 1 integrin signals. J Biol Chem. 2012 Aug 17;287(34):28586-97. doi: 10.1074/jbc.M112.350488.

60. Maugis D Adhesion of spheres: the JKR-DMT transition using a Dugdale model. J Colloid Interface Sci 150(1):243–269

61. Leckband D., Israelachvili J. Intermolecular forces in biology. Q Rev Biophys 34(2):105–267 2001

62. Heck T, Vargas DA, Smeets B, Ramon H, Van Liedekerke P, Van Oosterwijck H. The role of actin protrusion dynamics in cell migration through a degradable viscoelastic extracellular matrix: Insights from a computational model. PLOS Computational Biology 16(1): e1007250. https://doi.org/10.1371/journal.pcbi.1007250

63. P. Van Liedekerke, A. Buttenschoen, and D. Drasdo, "Off-lattice agent-based models for cell and tumor growth: Numerical methods, implementation, and applications," in *Numerical Methods and Advanced Simulation in Biomechanics and Biological Processes*, Miguel Cerrolaza Sandra Shefelbine Diego Garzón-Alvarado, 2017.

64. Smeets B, Odenthal T, Keresztes J, Vanmaercke S, Van Liedekerke P, Tijskens E, Saeys W, Van Oosterwyck H, Ramon H. Modeling contact interactions between triangulated rounded bodies for the discrete element method Computer Methods in Applied Mechanics and Engineering; 2014, 227

65. Boal D. Mechanics of the Cell. 2nd ed. Cambridge University Press; 2012.